Three-dimensional instabilities of a stratified cylinder wake

M Bosco, P Meunier

Three-dimensional instabilities of a stratified cylinder wake

By M. Bosco & P. Meunier

Aix-Marseille Univ., CNRS, Centrale Marseille, IRPHE, F-13384 Marseille, France

(Received 13 December 2013)

This paper describes experimentally, numerically and theoretically how the 3D instabilities of a cylinder wake are modified by the presence of a linear density stratification. The first part is focused on the case of a cylinder with a small tilt angle between the cylinder's axis and the vertical. The classical mode A well-known for a homogeneous fluid is still present. It is more unstable for moderate stratifications but it is stabilized by a strong stratification. The second part treats the case of a moderate tilt angle. For moderate stratifications, a new unstable mode appears, characterized by undulated layers of strong density gradients and axial flow. These structures correspond to Kelvin-Helmholtz billows created by the strong shear present in the critical layer of each tilted von Karman vortex. The last two parts deal with the case of a strongly tilted cylinder. For a weak stratification, an instability appears far from the cylinder, due to the overturning of the isopycnals by the von Karman vortices. For a strong stratification, a short wavelength unstable mode appears, even in the absence of von Karman vortices. It is probably due to the strong shear created by the lee waves upstream of a secondary recirculation bubble. A map of the four different unstable modes is established in terms of the three parameters of the study: the Reynolds number, the Froude number (characterizing the stratification) and the tilt angle.

1. Introduction & Context

Although the dynamics of a cylinder wake is well-known for a homogeneous fluid, there are very few studies for a stratified fluid. This paper analyzes the transition from a 2D von Karman street to 3D instabilities in a stratified cylinder wake, based on experimental evidences and with some numerical clues of the structures observed.

Bluff body wakes have been a main subject of interest for engineers due to their applications to terrestrial and naval vehicles, where drag reduction has been a major concern for cars, trains and boats. Bluff body wakes have also direct engineering significance for civil constructions, where the presence of alternated vortices in the wakes may cause structural vibrations leading to catastrophic failures. It would be difficult and not very universal to study complex-geometry body wakes such as cars, boats, buildings and bridges. However a simple geometry like a circular cylinder presents all the main characteristics of bluff body wakes (boundary layer separation, von Karman street, 3D instabilities, transition to turbulence). This is why this basic geometry is often used for fundamental studies on bluff body wakes.

The 2D dynamics of a cylinder wake has been largely studied in the last century. At low Reynolds number the flow is stationary and is characterized by a steady recirculation bubble behind the cylinder. A 2D periodic structure appears for $\mathrm{Re} \geqslant 50$ with the presence of alternate vortices which remain discernible even in a turbulent wake (see Williamson 1996a, for a review). The vortex street was primarily observed experimentally by Hiemenz and showed to be stable for point vortices for a specific aspect ratio of wavelength over distance between rows by von Karman (1912). This transition from a steady recirculation bubble to the periodic von Karman street was deeply investigated and thanks to Mathis *et al.* (1984), it was discovered that the transition is a Hopf bifurcation well modeled by a Landau equation (Landau & Lifchitz 1971). The parameters

were measured experimentally (Provansal *et al.* 1987; Schumm *et al.* 1994; Albarede & Provansal 1995), but also numerically (Jackson 1987; Noack & Eckelmann 1994; Dusek *et al.* 1994).

For higher Reynolds number, the dynamics of the cylinder wake is strongly modified due to the appearance of three-dimensional instabilities. The first unstable mode, called mode A, has been observed experimentally (Hama 1957; Bloor 1964; Williamson 1996b, 1988; Zhang *et al.* 1995; Norberg 1994) and also by Direct Numerical Simulations (Karniadakis & Triantafyllou 1992; Zhang *et al.* 1995; Henderson 1997; Thompson *et al.* 1994, 1996). The critical Reynolds number at which the mode becomes unstable varies between 150 and 190 (Williamson 1988; Karniadakis & Triantafyllou 1992; Zhang *et al.* 1995; Williamson 1996a). This large range is probably due to oblique shedding in the experiments and due to the fact that the transition is slightly subcritical (Henderson 1997; Behara & Mittal 2010). However, Barkley (1996) showed by a Floquet analysis that the mode A becomes linearly unstable at a critical Reynolds number $\mathrm{Re} = 188.5 \pm 1.0$ at a spanwise wavelength equal to 3.96 ± 0.02 diameters. This is in excellent agreement with the experiments and the DNS. The mode A seems to be the result of an elliptic instability of the von Karman vortices, as claimed by Williamson (1996b), Leweke & Williamson (1998) and Thompson *et al.* (2001), since it gives correct predictions of the spatial structure and of the wavelength.

At a Reynolds number larger than 230, a new unstable mode, called mode B, emerges with smaller-scale irregular patterns (Williamson 1988; Zhang *et al.* 1995; Henderson 1997). This mode is also predicted by the Floquet analysis of Barkley (1996) at a critical Reynolds number equal to 259 and a wavelength equal to 0.82 diameters. Wu *et al.* (1996) showed experimentally that this mode contains strong longitudinal vortices. This suggests that this mode B is due to the stretching of vorticity by the stagnation points of the

two-dimensional base flow located between two von Karman vortices, as in the case of the wake of a flat plate (Meiburg & Lasheras 1988). Mode A and B have a different symmetry: the longitudinal vortices rotate in the same direction at each half-wavelength for mode B, whereas they rotate in opposite direction at each half-wavelength for mode A (Williamson 1996a). The bifurcation due to the unstable mode B is supercritical (Henderson 1997). Mode B is present together with mode A until $\mathrm{Re} = 260$. Above this Reynolds number, the mode B becomes dominant. This coexistence of two modes can be modeled theoretically by two coupled non-linear Landau equations (Barkley *et al.* 2000), which allow to predict the Strouhal number as a function of the Reynolds number (Sheard *et al.* 2003).

Although the homogeneous dynamics of a cylinder wake has been extensively studied, very few papers have focused on stratified wakes despite obvious applications to geophysical flows and submarine wakes. Given that oceans and the atmosphere are stratified, most environmental flows like island wakes and mountain range wakes are strongly influenced by the mean density gradient. Besides, the stable oceanic stratification is a key ingredient for naval applications such as submarine wakes. This interest has resulted in laboratory investigations of the turbulent regime of a bluff body with a finite height like a sphere, a spheroid or a streamwise cylinder at large Reynolds number. The early paper of Lin & Pao (1979) showed that the isotropic wake becomes quasi-2D with a saturation of the height after a time inversely proportional to the Brunt-Väisälä frequency N. Large horizontal vortices with limited vertical scale are created. They grow in width by merging together which gives rise to an algebraic growth of the wake width and an algebraic decay of the velocity. The scaling laws for the width and the velocity have been established for a sphere by Spedding (1997) and extended to different geometries by Meunier & Spedding (2004). The exponents were recovered theoretically by Meunier & Spedding (2006) who assumed that the Reynolds stress is proportional to the mean shear. Diamessis *et al.*

(2011) finally showed that at large Reynolds number, Kelvin-Helmholtz billows are created at the top and the bottom of the horizontal vortices. It was shown by Brucker & Sarkar (2010) that the wake of a self-propelled body decays faster in the early stages but slower in the late stages, as observed experimentally by Meunier & Spedding (2006). However, in practice, the presence of a small acceleration introduces some momentum which governs the dynamics of the wake (Meunier & Spedding 2006).

Stratified wakes of a horizontal cross-stream cylinder have received even less attention. Boyer *et al.* (1989) discovered a large variety of regimes when the Froude number varies from 0.02 to 13 and the Reynolds number varies from 5 to 4000. For strong stratification, they revealed the presence of internal waves, of an accelerated flow on the centerline and of isolated recirculation bubbles downstream of the cylinder. The flow also creates a recirculating bubble upstream of the cylinder, which is known as the blocking effect studied by Browand & Winant (1972), Baines (1987), Xu *et al.* (1995) and Winters & Armi (2012). When the Reynolds number increases, Boyer *et al.* (1989) showed that the flow transitions to vortex shedding and to a turbulent flow. But the stratification tends to prevent the appearance of von Karman vortices, due to the stabilization of shear flows by a stratification. This effect can be quantified by the Richardson criterion, leading to the dependence of the critical Reynolds number with the Froude number (Meunier 2012).

However, the dynamics of the wake is strongly modified when the cylinder is no longer horizontal but tilted with respect to the vertical. Indeed, Meunier (2012) showed experimentally and numerically that von Karman vortices can be emitted for strong stratifications at moderate Reynolds numbers. This is in agreement with the new unstable mode found by Candelier *et al.* (2011) in a tilted jet using a linear stability analysis. The existence of tilted vortices in a strongly stratified fluid is made possible because the streamlines remain horizontal but centered around a tilted axis (Boulanger *et al.* 2006;

Canals *et al.* 2009). However, this structure generates a critical layer at the radius where the angular velocity equals the Brunt-Väisälä frequency, leading to strong axial shears which are unstable with respect to the Kelvin-Helmholtz instability (Boulanger *et al.* 2007).

To conclude, the 3D instabilities of a stratified cylinder wake have been only briefly studied. Moreover, they focused on the case of a horizontal cylinder despite the strong influence of the tilt angle. The goal of the paper is thus to characterize this transition experimentally for all tilt angles and Froude numbers.

The paper will be organized as follows. In section 2, we describe the experimental set-up and the reduced governing equations. Section 3 is devoted to the mode A, well-known in the case of a homogeneous fluid, for a nearly vertical cylinder. Section 4 presents another instability mode appearing for a moderate tilt angle. The case of a nearly horizontal cylinder is finally treated, for a weak stratification (Section 5) and for a strong stratification (Section 6). Conclusions follow in section 7.

2. Materials and methods

2.1. *Experimental details*

The model experiment used to study the dynamics of a stratified cylinder wake is presented schematically in figure 1. A 150 cm long, 75 cm wide and 50 cm high Plexiglas tank is built in order to make visualizations from all sides.

The tank contains a stable linearly stratified fluid in salt up to a height Z = 40 cm obtained by the double bucket method. The water from the first bucket (filled with salted water at a density $\rho = 1.15$kg/l) is slowly deposited at the surface of the tank using a floater. The density of the first bucket is gradually decreased by the addition of fresh water from a second bucket. The density gradient is obtained from density

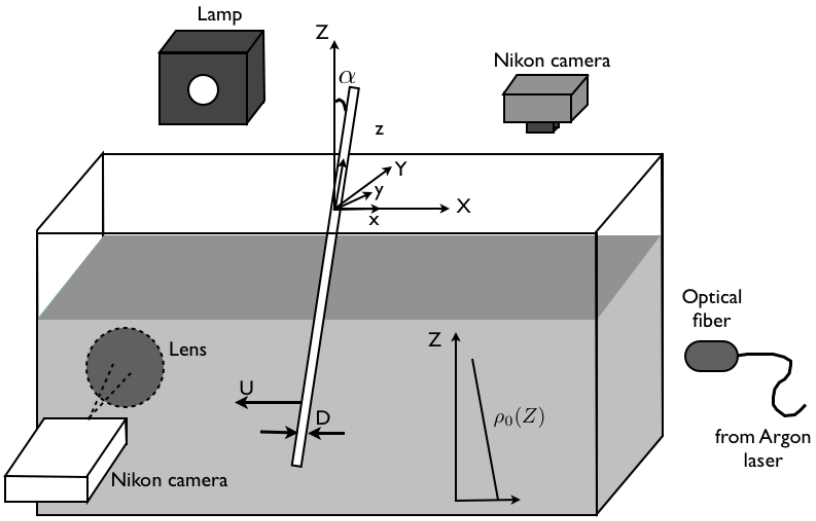

FIGURE 1. Schematic of the experimental set-up: the stratified cylinder wake is analyzed by dye visualizations on the right side and by shadowgraph method on the left side.

measurements of small samples of fluid every 10 cm, using a densitometer Anton Paar DMA 35N with an accuracy of 10^{-4} kg/l. The typical Brunt-Väisälä frequency defined by $N = \sqrt{(-g/\rho)(\partial\rho/\partial Z)}$ is close to 2 rad/s. The stratification can stay linear during approximately two months except at the top and the bottom of the tank because of mixing at the extreme layers. Fresh water is weekly deposited at the free layer so as to reduce the evaporation effect.

To study the dynamics, a circular cylinder of diameter D is introduced in the tank. This cylinder is towed horizontally in the stratified fluid, at a velocity U varying between 0.5 cm/s and 5 cm/s. The diameter varies between 0.3 cm and 1.8 cm. The cylinder can be tilted relative to the vertical, at an angle α in the cross-stream plane as can be seen on figure 1. The cylinder is mounted on a carriage translated along horizontal rails, entrained by a belt driven by a DC motor coupled to a 1: 90 reductor. The towing velocity is stable within 0.1% even at low speed.

As shown on Fig. 1, two visualization methods are used. The first one is the shadow-

graph method which reveals non-uniformities in the water tank. On a side of the tank, a light is placed far from the tank in order to create parallel light which goes through the experiment and whose rays are deviated by refraction. A lens and a camera located at the focal distance are placed at the other side of the tank. The deviated rays do not enter the camera, creating dark areas on the images, which thus reveal the density gradients. The other visualization method consists in depositing a fluorescent dye mixture made of Fluorescein and silicon on the upstream side of the cylinder. Once the dye is dry, the cylinder is slowly lowered into the water without disturbing the fluid. During the experiment, the dye is advected by the flow and detaches at the separation point together with the vorticity. These methods are used to determine the stability of the flow and to measure the wavelength and recirculation length of the wake.

The stratified wake of the tilted cylinder is characterized by four non-dimensional parameters: the cross-stream tilt angle α, the Reynolds number Re, the Froude number F and the Schmidt number Sc. However, the last parameter defined as $\mathrm{Sc} = \nu/\kappa = 700$ (κ being the diffusivity of salt in water) is large in this study, which reduces the problem to 3 main non-dimensional parameters.

The tilt angle α varies between 0° and 90°. The Reynolds number $\mathrm{Re} = UD/\nu$ is varied between 30 and 300. In our experiments, the kinematic viscosity ν increases by 10% from the top to the bottom due to the presence of salt, which introduces an error on the Reynolds number of 5%. There is no temperature variation with the depth but the temperature was measured within half a degree in order to be accurate within 2% for the mean Reynolds number. The Froude number F = U/ND, is varied between 0.5 and 8 by changing the diameter D and the velocity of the cylinder simultaneously. The stratification length L defined by $L = \rho_0/(\partial\bar{\rho}/\partial z)$ quantifies the non-Boussinesq effects,

which are proportional to 1/L. Since L is very large in our experiments ($L \simeq 300$), the whole study is thus done under the Boussinesq approximation.

2.2. *Numerical formulation of the problem*

The flow is governed by the Navier-Stokes equations coupled with the density equation and the incompressibility condition:

$$\frac{D\mathbf{u}}{Dt} = -\frac{1}{\rho_0}\nabla p + \frac{\rho}{\rho_0}\mathbf{g} + \nu\triangle\mathbf{u} \tag{2.1a}$$

$$\frac{D(\bar{\rho}+\rho)}{Dt} = \kappa\triangle\rho \tag{2.1b}$$

$$\nabla\cdot\mathbf{u} = 0 \tag{2.1c}$$

These equations are written in the Boussinesq approximation where the density perturbation ρ and the mean density profile $\bar{\rho}(Z)$ are smaller than the absolute density ρ_0 and where the static pressure is removed. The problem is solved in the frame of reference moving with the cylinder. The translation of the fluid is thus imposed by the boundary conditions at infinity: $u = U$ and $v = w = \rho = 0$. At the surface of the cylinder ($r = D/2$), no-slip boundary conditions are imposed for the velocity ($u = v = w = 0$) and the normal flux of density is taken equal to zero ($\partial\rho/\partial n = 0$). The towing velocity U, the cylinder diameter D and the mean density ρ_0 permit to dimensionalize the problem. Thus lengths are dimensionalized by D, times by D/U and mass by $\rho_0 D^3$. The study is solved in the tilted frame of reference $(Oxyz)$ of the cylinder, whose axes are tilted by an angle α compared to the vertical/horizontal axes of $(OXYZ)$, as sketched on figure 1. The gravity $\mathbf{g}$ is thus splitted onto the y and z components. Moreover, the term $D\bar{\rho}/Dt$ contains both the y and z component of the velocity. In a first step, the 2D flow (i.e. invariant along the cylinder's axis) is calculated corresponding to the base flow. The 2D

flow is governed by 5 equations for the velocity $(u_{2\mathrm{D}}, v_{2\mathrm{D}}, w_{2\mathrm{D}})$, pressure $p_{2\mathrm{D}}$ and density $\rho_{2\mathrm{D}}$ depending on x and y only:

$$\frac{\tilde{D}u_{2\mathrm{D}}}{\tilde{D}t} = -\frac{\partial p_{2\mathrm{D}}}{\partial x} + \frac{1}{\mathrm{Re}}\triangle u_{2\mathrm{D}} \tag{2.2a}$$

$$\frac{\tilde{D}v_{2\mathrm{D}}}{\tilde{D}t} = -\frac{\partial p_{2\mathrm{D}}}{\partial y} + \frac{\rho_{2\mathrm{D}}\sin\alpha}{F^2} + \frac{1}{\mathrm{Re}}\triangle v_{2\mathrm{D}} \tag{2.2b}$$

$$\frac{\tilde{D}w_{2\mathrm{D}}}{\tilde{D}t} = -\frac{\rho_{2\mathrm{D}}\cos\alpha}{F^2} + \frac{1}{\mathrm{Re}}\triangle w_{2\mathrm{D}} \tag{2.2c}$$

$$\frac{\tilde{D}\rho_{2\mathrm{D}}}{\tilde{D}t} = w_{2\mathrm{D}}\cos\alpha - v_{2\mathrm{D}}\sin\alpha + \frac{1}{\mathrm{Re}Sc}\triangle\rho_{2\mathrm{D}} \tag{2.2d}$$

$$\frac{\partial u_{2\mathrm{D}}}{\partial x} + \frac{\partial v_{2\mathrm{D}}}{\partial y} = 0 \tag{2.2e}$$

In these equations, the density $\rho_{2\mathrm{D}}$ has been further dimensionalized by the non-dimensional stratification length L and $\tilde{D}/\tilde{D}t = \partial/\partial t + u_{2\mathrm{D}}\partial/\partial x + v_{2\mathrm{D}}\partial/\partial y$ corresponds to the 2D Lagrangian derivative in the plane perpendicular to the cylinder. Since there is no advection term $w_{2\mathrm{D}}\partial/\partial z$ for a 2D flow, the problem can be treated as a two-dimensional flow for $(u_{2\mathrm{D}}, v_{2\mathrm{D}})$ depending on x and y only with two active scalars $w_{2\mathrm{D}}$ and $\rho_{2\mathrm{D}}$. The forcing term in the second equation is considered as a volumic force and the forcing terms in the third and fourth equations are considered as creation rates of the scalars $w_{2\mathrm{D}}$ and $\rho_{2\mathrm{D}}$.

In a second step, the 3D flow has been calculated in order to find the 3D unstable modes. The 3D flow is simply modeled as a sinusoidal perturbation of wavenumber k added to the base flow:

$$\begin{cases} u(x,y,z) = u_{2\mathrm{D}}(x,y) + u_1(x,y)\cos kz - u_2(x,y)\sin kz \\ v(x,y,z) = v_{2\mathrm{D}}(x,y) + v_1(x,y)\cos kz - v_2(x,y)\sin kz \\ w(x,y,z) = w_{2\mathrm{D}}(x,y) + w_1(x,y)\sin kz + w_2(x,y)\cos kz \\ p(x,y,z) = p_{2\mathrm{D}}(x,y) + p_1(x,y)\cos kz - p_2(x,y)\sin kz \\ \rho(x,y,z) = \rho_{2\mathrm{D}}(x,y) + \rho_1(x,y)\sin kz + \rho_2(x,y)\cos kz \end{cases} \tag{2.3}$$

This decomposition is introduced in the Navier-Stokes equations (2.1) which are linearized for the 3D perturbations $\mathbf{u_1}$ and $\mathbf{u_2}$. Separating the Fourier components leads to 3 systems of equations for the base flow and the two perturbations. The system of equations for the base flow is similar to the 2D case and is given by (2.2).

The equations governing the perturbation $(u_1, v_1, w_1, p_1, \rho_1)$ can be written as follows:

$$\frac{\tilde{D}\mathbf{u_1}}{\tilde{D}t} + (\mathbf{u_1}\cdot\tilde{\nabla})\tilde{\mathbf{u}}_{2\mathrm{D}} + \epsilon_1[(\mathbf{u_2}\cdot\tilde{\nabla})(w_{2\mathrm{D}}\mathbf{e_z}) - kw_{2\mathrm{D}}\mathbf{u_2}] = -(\tilde{\nabla}p_1 - kp_1\mathbf{e_z}) + \frac{\tilde{\triangle}-k^2}{\mathrm{Re}}\mathbf{u_1} + R_1$$

$$\tilde{\nabla}\cdot\mathbf{u_1} + kw_1 = 0$$

$$\frac{\tilde{D}\rho_1}{\tilde{D}t} + \epsilon_1[kw_{2\mathrm{D}}\rho_2 - (\mathbf{u_2}\cdot\tilde{\nabla})\rho_{2\mathrm{D}}] = \frac{\tilde{\triangle}-k^2}{ReSc}\rho_1 + w_1\cos\alpha + \epsilon_1 v_2\sin\alpha$$

Here $R_1 = (0, \epsilon_1\rho_2\sin\alpha, -\rho_1\cos\alpha)/F^2$ corresponds to the buoyancy force, $\epsilon_1 = 1$ and $\mathbf{e_z}$ is the axial unitary vector. $\tilde{D}/\tilde{D}t = \partial_t + \tilde{\mathbf{u}}_{2\mathrm{D}}\cdot\nabla$ corresponds to the 2D Lagrangian derivative with $\tilde{\mathbf{u}}_{2\mathrm{D}} = (u_{2\mathrm{D}}, v_{2\mathrm{D}}, 0)$ the cross-cut component of the base flow. We have also defined the 2D divergence $\tilde{\nabla} = (\partial_x, \partial_y, 0)$ and the 2D Laplacian operator $\tilde{\triangle} = \partial^2/\partial x^2 + \partial^2/\partial y^2$. The system of equations for the second perturbation $(u_2, v_2, w_2, p_2, \rho_2)$ is simply obtained by inverting indices 1 and 2 with $\epsilon_2 = -1$.

Numerically, the problem is solved in a square rectangle with $x \in [-4, 16]$ and $y \in$

$[-5, 5]$, the cylinder being centered at $(x = 0, y = 0.1)$. The small y-offset allows to break the symmetry of the numerical wake and thus prevents the solution to lock on a stable wake. The boundary conditions on the outer rectangle are slightly different than in the theoretical problem. At the entrance of the flow ($x = -4$), the velocity is imposed as $(u_{2D}, v_{2D}, w_{2D}) = (1, 0, 0)$ and the density is equal to 0. On the side walls ($y = \pm 5$), slip boundary conditions for the (u, v) velocity are used and no outward flux of density and vertical velocity w is imposed. At the exit of the flow ($x = 16$), the boundary is assumed to exert no force on the fluid (stress tensor equal to zero) and there is no diffusive flux of density and vertical velocity ($\partial\rho/\partial x = \partial w/\partial x = 0$). At the surface of the cylinder, the boundary conditions are taken as previously stated: no-slip boundary conditions for the velocity and no normal flux of density. Moreover the boundary conditions verified by the 3D perturbations $\mathbf{u_1}$ and $\mathbf{u_2}$ are similar to the base flow.

The study is solved using Comsol Multiphysics ©, which is a finite element method allowing to couple several partial differential equations. The numerical study is initiated with the two-dimensional dynamics. Once the von Karman wake is fully developed, we solve simultaneously the equations for the 3D perturbations. When the flow is unstable, the numerical noise is sufficient to give an exponential growth of the perturbation. The initial conditions can be taken either with zero initial flow or as the flow previously obtained at different parameters (higher or smaller Reynolds number for example). This allows to measure negative growth rates when the 3D perturbation decays exponentially. The mesh contains 13072 elements and Lagrange elements are used for each variable. The time-dependent simulations are solved by a direct (UMFPACK) method with self-adaptive time steps. The simulations are carried out on a long time (up to $t = 500$ in dimensionless units) to allow the von Karman instability to grow and saturate. This could take up to 4 hours of computation for one set of parameters on a Mac Book Pro.

3. Mode A: The instability of nearly vertical cylinders

In this section, we focus on the stability of the wake when the cylinder is vertical or weakly tilted.

3.1. *Shadowgraph visualisations*

For large Froude numbers, the 2D wake is destabilized when the Reynolds number increases above 190. Figure 2 shows the periodic structures with a well-defined wavelength which are created about 5 diameters downstream of the cylinder. These structures are characteristic of the classical mode A, well-known in a homogeneous fluid. Indeed, the sideview is very similar to the dye visualization of Fig. 13 in Williamson (1996a), with longitudinal vortices whose tails are stretched toward the cylinder. The front view of Fig. 2(b) clearly shows that these vortices are counter-rotating vortex pairs perpendicular to the von Karman vortices.

Moreover, the wavelength of this mode is close to 4 diameters, which is in excellent agreement with the theoretical value $\lambda/D = 3.96 \pm 0.02$ obtained by Barkley (1996) for the mode A. The wavelength of this mode has been measured for different Froude numbers and is plotted in Fig. 3. It seems to be independent of the Froude number within the noise in the measurement (of the order of 20%).

This mode A is the first 3D unstable mode when the cylinder is tilted with an angle smaller than 45°. The spatial structure is very similar for a tilted cylinder and the wavelength remains unchanged, as can be seen on Fig. 3. However, the critical Reynolds number strongly varies with the Froude number and the tilt angle as will be shown in the next section.

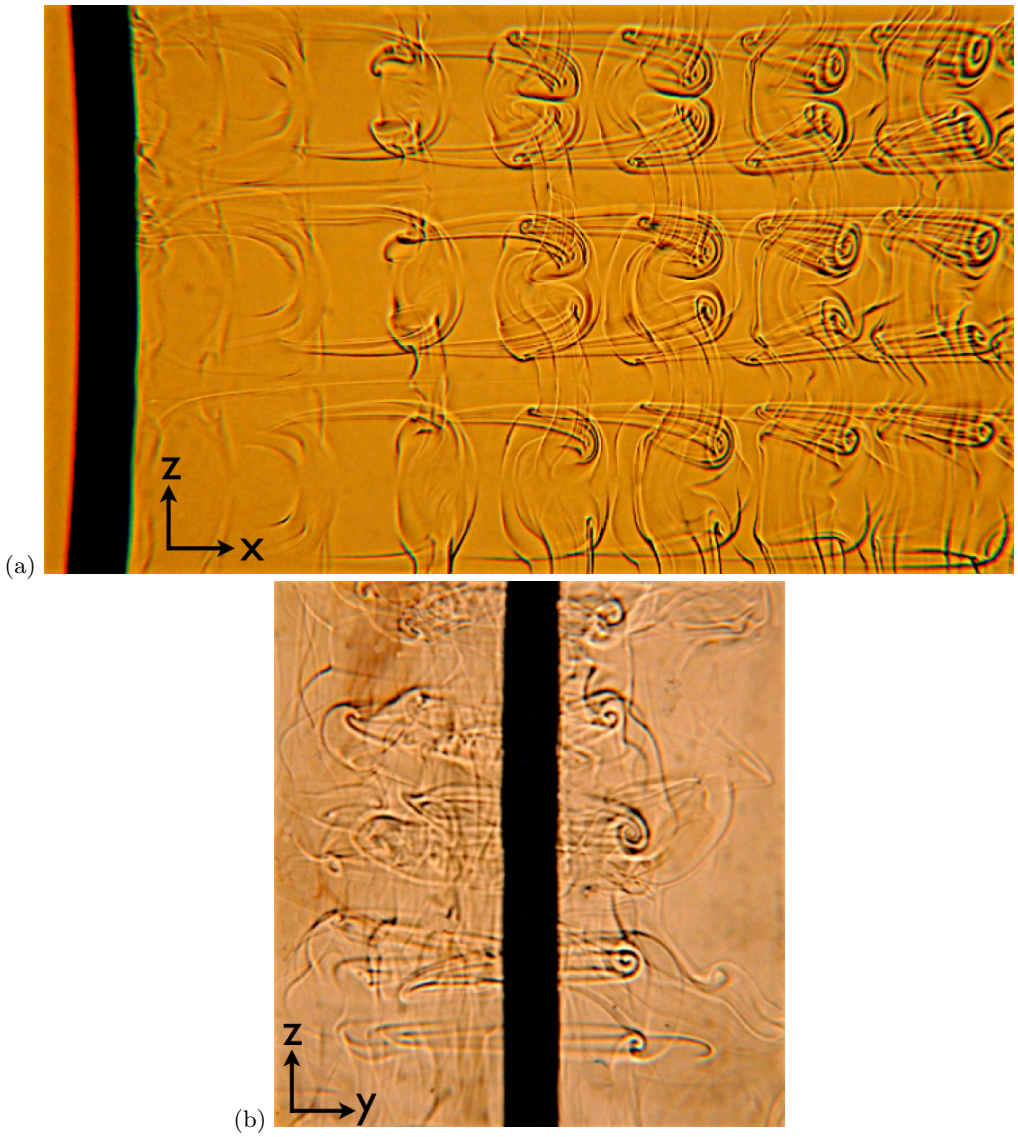

FIGURE 2. Shadowgraph visualizations of the wake behind a vertical cylinder obtained at the same Reynolds number Re = 190 and Froude number F = 4. In the side view (a), the cylinder is going to the left. In the front view (b) the cylinder is going toward the observer with a very small angle in order to see the structures on the right side of the cylinder. The field of view is approximately 8 by 15 diameters in the sideview.

3.2. *Stability diagram*

By varying the velocity and the diameter of the cylinders, it is possible to vary independently the Reynolds number and the Froude number. We have done different experiments

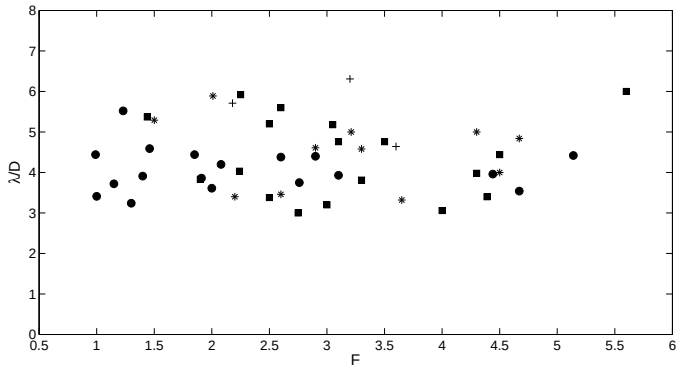

FIGURE 3. Plot of the wavelength λ of the mode A dimensionalized by D for different values of Froude numbers at a Reynolds number between 180 and 190, for different tilt angles α. Disks are experimental points obtained for the vertical cylinder, squares for $\alpha = 30°$, crosses for $\alpha = 45°$ and stars for $\alpha = 60°$.

in order to determine the stability of the 2D flow as a function of the Reynolds number and the Froude number. These results are reported in Fig. 4, where circles correspond to a 2D flow and stars correspond to mode A. This stability diagram allows to determine the critical Reynolds number Re_c at which the flow becomes 3D as a function of the Froude number (plotted as a solid line). At large Froude number, the critical Reynolds number tends to $Re_c = 185 \pm 5$. This result is satisfying because for these weak stratifications, the dynamics of the wake is expected to be the same than for a homogeneous cylinder wake, where the critical Reynolds number is equal to 189 (Barkley 1996).

For moderate Froude numbers ($1 \leqslant \mathrm{F} \leqslant 4$), the critical Reynolds number decreases with a minimum of $\mathrm{Re}_c = 130$ at $F = 1.5$. This indicates that a moderate stratification seems to destabilize the 3D mode A. This is surprising because the stratification is known to stabilize the elliptical instability, which is claimed to be at the origin of mode A (Leweke & Williamson 1998; Williamson 1996b; Thompson *et al.* 2001). Indeed, Kerswell (2002) showed using a local approach that the growth rate σ of the elliptical instability is given

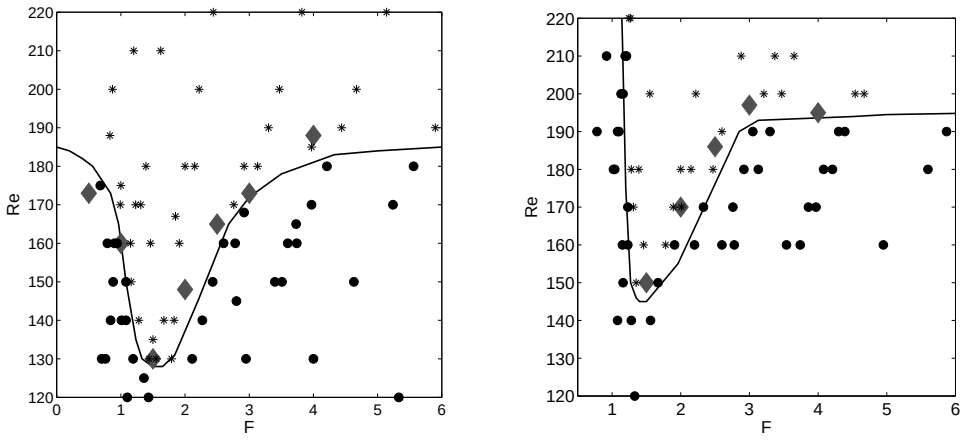

(a) (b)

FIGURE 4. Stability diagrams of the 3D instabilities in the stratified wake of (a) a vertical cylinder and (b) a cylinder tilted at an angle $\alpha = 30^\circ$ in the cross-stream section. Black round symbols correspond to stable experiments and stars correspond to the mode A. The solid line corresponds to the limit of stability found experimentally. Grey diamonds correspond to the critical Reynolds number obtained numerically.

by

$$\sigma = \frac{9}{16}\epsilon(1 - \frac{3}{4F_v^2})$$

in the presence of a weak stratification. Here, the vortex Froude number $F_v = \Omega_0/N$ is based on the angular velocity Ω_0 at the core of the vortex and ϵ corresponds to the ellipticity of the streamlines. This equation indicates that the growth rate decreases in the presence of a weak stratification, which would correspond to a stabilization of the mode A. This is opposite to the experimental observations where a weak and moderate stratification destabilizes the mode A.

To understand this difference, we have calculated analytically the growth rate of the elliptical instability for a Gaussian vortex in a stratified fluid, using a global approach instead of the local approach used by Kerswell (2002). The calculation, detailed in the appendix, is very similar to the calculation done in Guimbard *et al.* (2010) for the elliptic

flow in a rotating stratified cylinder. Unfortunately, the analytical growth rate is very close to the local theory and leads to the same conclusion, i.e. a stabilization for weak stratification. A possible explanation for this discrepancy may be due to the fact that the elliptical instability is calculated for a single vortex whereas the mode A is a global mode for the whole von Karman vortex street. It is indeed possible that the group velocity of the 3D perturbation increases with the stratification such that the instability becomes absolutely unstable for smaller Reynolds numbers than without stratification.

However, when the Froude number is decreased below 1.5 the stratification has a drastic stabilization effect. Indeed the critical Reynolds number strongly increases by 50% between $F = 1.5$ and $F = 0.5$. This is probably due to the appearance of critical layers in the Kelvin modes of a stratified Gaussian vortex, which creates a strong dissipation (Le Dizès 2008).

When the cylinder is slightly tilted in the cross-stream section ($0° \leqslant \alpha \leqslant 30°$), the mode A is still observed. The stability diagram has also been established for $\alpha = 30°$ (see figure 4b). The variation of the critical Reynolds number with the Froude number is similar to the case of the vertical cylinder. Mode A is destabilized for $1.5 < F < 4$ and stabilized for $F < 1.5$. However, the destabilization is weaker for the tilted cylinder (with a minimum $\mathrm{Re}_c = 150$) than for the vertical case (with a minimum $\mathrm{Re}_c = 130$). This indicates that the tilt of the cylinder tends to stabilize the mode A. This is even clearer at larger angle as will be shown in section 4.

3.3. *Numerical simulation*

The critical Reynolds number has also been calculated numerically using the Navier-Stokes equations linearized around the 2D base flow. The perturbation is assumed to be sinusoidal in z, with a fixed wavenumber k, as given by (2.3). This method is similar to the Floquet analysis done by Barkley (1996). Figure 5 is an example of the numerical result

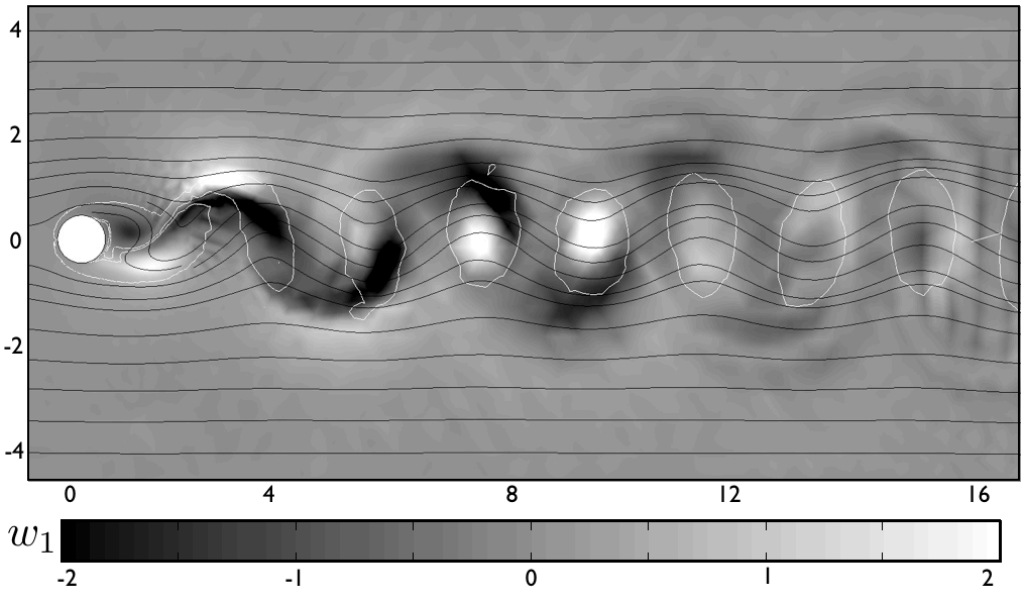

FIGURE 5. Axial velocity of the 3D perturbation w_1 obtained numerically for a vertical cylinder in the (x, y) plane at Re = 190 and $F = 4$. Solid lines are the streamlines of the 2D flow (u, v) corresponding to a von Karman street. Black and white contour lines correspond to the vorticity. The field of view is 16 by 6 diameters.

obtained by Comsol. In this figure, the black and white contours of vorticity indicate the position of the 2D von Karman vortices and the greyscales correspond to the axial velocity of the 3D perturbation w_1. In each vortex, there are two lobes of axial velocity, one positive and one negative. This is especially visible in the second and third vortices. It corresponds to the spatial structure of the elliptic instability, as noted by Thompson *et al.* (2001) for mode A.

In order to determine the growth of the perturbation, the axial velocity w_1 is measured at $x = 5$ and $y = 0.5$, i.e. at the position where the maximum of axial velocity passes periodically. It is plotted in Fig. 6 as a function of time and indeed exhibits periodic peaks of velocity. Moreover, the amplitude of these peaks increases exponentially with time and grows by almost one decade between $t = 0$ and $t = 70$. Fitting the maxima

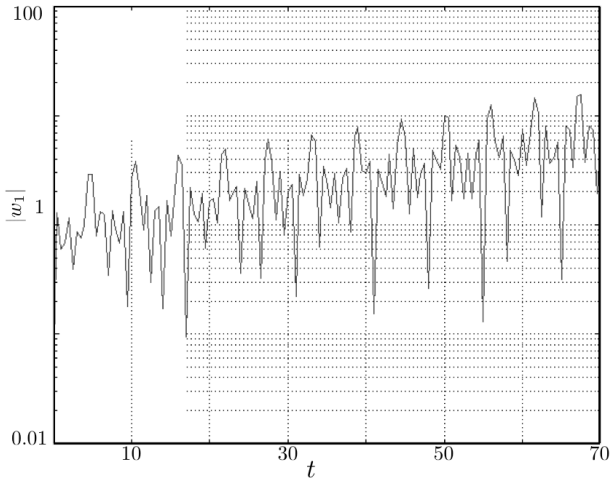

FIGURE 6. Temporal variation of the absolute value $|w_1|$ of the axial velocity of the perturbation. The velocity is evaluated at $(x, y) = (5, 0.5)$. Re $= 220$, $F = 3$.

with an exponential function $\exp(\sigma t)$ allows to determine the growth rate σ for a given Reynolds number, Froude number and wavenumber.

To determine the critical Reynolds number, the maximal wavenumber $k_{\max}$ corresponding to the most unstable mode is searched for each Froude number and Reynolds number. To do so, the instability growth rate σ is measured for three values of k around the maximum and fitted by a parabola. In fact, it was found that $k_{max} \simeq 1.5$ is almost independent of the Froude and the Reynolds number, in agreement with the experimental results. Then, the maximum growth rate σ is calculated for different values of Reynolds number. As shown on figure 7, it increases linearly with the Reynolds number. The critical Reynolds number Re_c simply corresponds to the Reynolds number at which the growth rate σ vanishes.

This critical Reynolds number is calculated for various Froude numbers F. It is plotted in Fig. 4 as grey diamonds. It is very close to the experimental critical Reynolds number (plotted as a solid line), although it seems to be slightly above the experimental value. This is probably due to the subcriticality of this transition which imposes that the linear

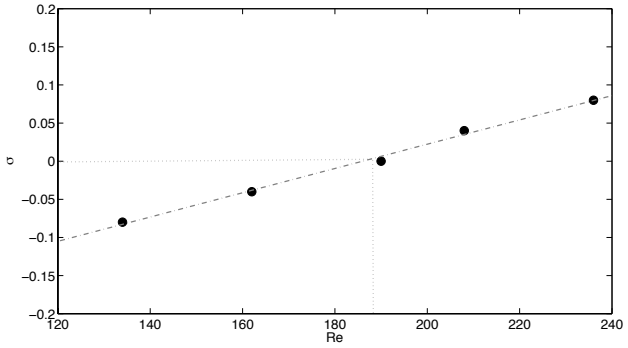

FIGURE 7. Growth rate of the instability for different Reynolds numbers at $F = 4$ with $k = k_{max} = 1.5$. Black symbols correspond to numerical data and the dashed line is a linear fit of the numerical points.

threshold is above the nonlinear threshold. However, the most important result is that the critical Reynolds number indeed decreases down to 130 when the Froude number is equal to 1.5. This is a good confirmation of the destabilization of the mode A by a weak to moderate stratification.

4. Mode S: The instability of tilted cylinders

4.1. *A new unstable mode*

The previous section showed that the mode A is the first unstable mode for weakly tilted cylinders. This dynamics is strongly modified when the tilt angle α is increased above 45°. Indeed, a new unstable mode appears in a region of moderate stratification ($1.5 \leqslant F \leqslant 3.5$). Figure 8 shows side shadowgraph views of this unstable mode, which is characterized by axial lines undulated at a well defined wavelength. It should be mentioned that for this tilt angle, the lines are present below the critical Reynolds number ($Re \leqslant 140$), but they remain straight. This indicates that these lines are created by the two-dimensional base flow. In the shadowgraph visualisations, they reveal layers of strong density gradients. It can be noted that they appear once dark and once white probably because the von

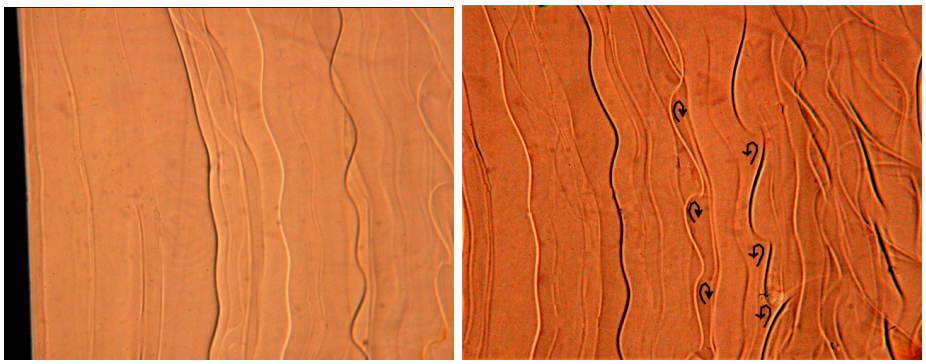

(a) (b)

FIGURE 8. Shadowgraph sideview visualizations of the wake behind a cylinder tilted at $\alpha = 45°$ for Re $= 170$ and $F = 2.5$. The cylinder is going to the left of the picture and there is a time delay of approximatively $6D/U$ between pictures (a) and (b) to reveal the temporal evolution of the instability. The field of view is approximately 8 by 15 diameters.

Karman vortices are alternate. Above the critical Reynolds number, these straight lines begin to undulate. The undulations grow with time describing S-shape structures far from the cylinder. This is why this mode has been called mode S. The dimensionless wavelength of this structure is $\lambda/D \simeq 4$ which is the same than for the mode A discussed previously.

The undulations seem to reveal lines of co-rotating vortices, as drawn schematically in Fig. 8(b). This could correspond to Kelvin-Helmholtz billows of a vertical shear layer. It should be noted that the shear is opposite between the white and the dark layers, since the vortices have opposite rotating directions.

4.2. *A tilt-induced instability*

In order to understand the structure and the origin of this instability, the 2D dynamics has been analyzed numerically using Comsol. Figure 9(a) shows that the 2D base flow is characterized by strong axial velocities which can be as large as the incoming flow. The axial velocity is confined in mushroom-like structures between the von Karman vortices.

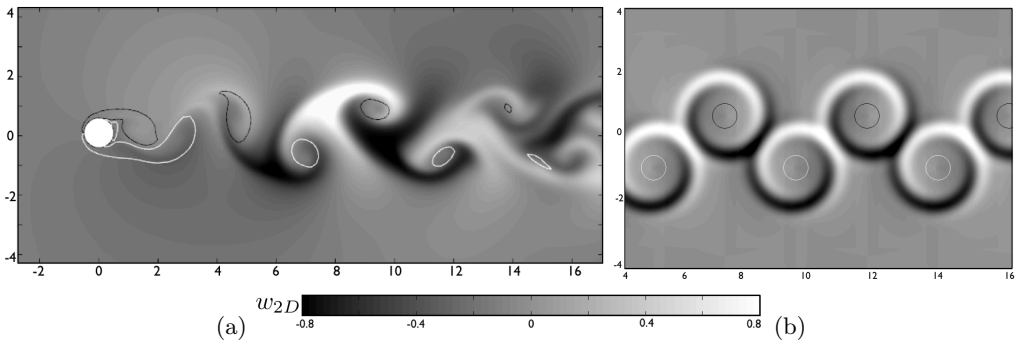

FIGURE 9. Axial velocity $w_{2\mathrm{D}}$ of the 2D base flow obtained (a) by a 2D numerical simulation and (b) for the axial flow generated by two lines of alternate vortices. The tilt angle $\alpha = 45°$, the Reynolds number $\mathrm{Re} = 180$ and the Froude number $F = 2.5$ are chosen where the mode S is observed experimentally. Black and white contours correspond to negative and positive vorticity.

The velocity is alternately positive and negative, which can explain the fact that the lines are alternately white and black in the shadowgraph visualizations of figure 8. These mushroom-like structures are actually due to the tilted vortices. Indeed, we show in the following that they can be explained by the critical layers appearing in each tilted vortex.

Boulanger *et al.* (2006) have shown that the inviscid solution of a solitary vortex (tilted with respect to the stratification) exhibits a divergence of the axial velocity at the critical radius r_c where the angular velocity of the vortex $\Omega(r_c)$ is equal to the Brunt-Väisälä frequency. Using a viscous critical layer analysis, they found that close to r_c, the velocity has the form:

$$w_{2\mathrm{D}}(r) = \frac{\pi r_c \Omega^2(r_c)}{|2\Omega'^2(r_c)|^{2/3}} H_i[i|2\Omega'^2(r_c)|^{1/3}(r - r_c)Re^{1/3}]$$

where $\Omega'(r_c)$ represents the derivative of the angular velocity and H_i corresponds to the Scorer function. This theoretical solution is plotted for each von Karman vortex in Fig. 9(b). To do so, the positions of the vortices are extracted from Fig. 9(a) and the profile of angular velocity is chosen as $\Omega(r) = \Gamma[1 - \exp(-r^2/a^2)]/(2\pi r^2)$ with $a = 0.7D$

and $\Gamma = \pm 2.31UD$ in order to represent the von Karman vortices of figure 9(a). It is clear that the interference of the critical layers generate mushrooms of axial velocity with alternately positive and negative sign, as in the numerical simulation. The amplitude of the axial velocity is of the same order in the theory and in the numerics. But the thickness of the structures seem to be larger in the numerics than in the theory. This is probably due to numerical diffusion inherent to the finite-element method used by Comsol.

A quantitative comparison of this model with the numerics can be done by plotting the maximum axial velocity $w_{2\mathrm{D}}^{\max}$ of the 2D base flow for different Froude numbers (Fig. 10a). It can be noted that $w_{2\mathrm{D}}^{\max}$ increases drastically at $F \simeq 1$. This transition corresponds to the appearance of the critical layer (which does not exist for small F because $\Omega(r) < N$ for all r). The maximum value of the axial velocity $w_{2\mathrm{D}}^{\max}$ is reached at $F \simeq 2$ and is slightly larger than 1. For larger Froude numbers, the axial velocity $w_{2\mathrm{D}}^{\max}$ decreases gradually. The theoretical prediction of $w_{2\mathrm{D}}^{\max}$ is plotted as a dashed-dotted line in Fig. 10(a). It is in good quantitative agreement with the numerics at small Froude numbers. However, this theory can only be used for moderate Froude numbers because at large Froude numbers the vortices cannot be considered as solitary, the critical layers being larger than the distance between vortices.

Figure 10(b) shows the maximum of the axial shear $\partial w_{2\mathrm{D}}/\partial x$. The shear suddenly increases at $F \simeq 1$ and reaches a maximum of the order of 5 at $F \simeq 2$. For larger F the shear gradually decreases. There is again a correct agreement between the theory and the numerics.

These results clearly prove that the strong axial velocity and strong shears present in the base flow are due to the critical layers of the von Karman vortices. Moreover, these high shears are largest for moderate Froude numbers ($1.5 < F < 4$), i.e. exactly where the mode S is observed in the experiments. This indicates that the mode S is simply a

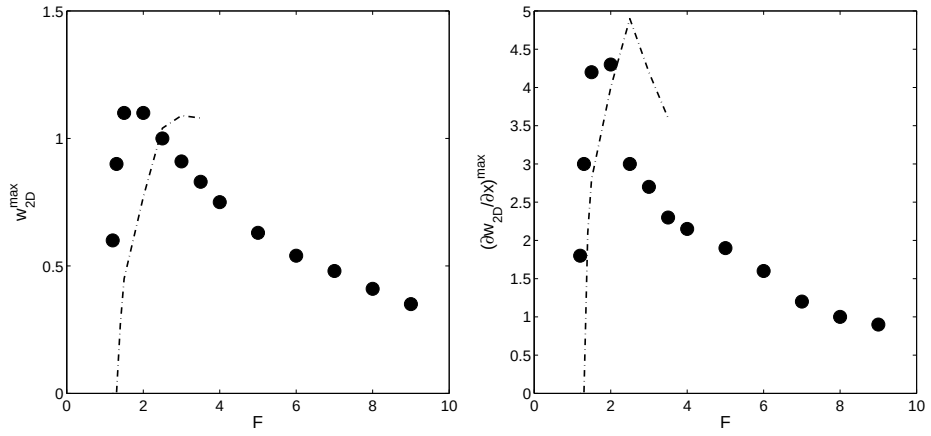

(a) (b)

FIGURE 10. Maximum value of (a) the axial velocity w_{2D} and (b) of the shear $\partial w_{2D}/\partial x$ as a function of the Froude number. Black symbols represent the numerical data and dashed lines represent the theoretical prediction. Re = 180, $\alpha = 45°$.

Kelvin-Helmholtz instability of these strong shears, as was observed for solitary tilted vortices by Boulanger *et al.* (2007). Indeed, the shear $\partial w_{2D}/\partial x$ generates cross-stream Kelvin-Helmholtz billows on an axial line, as observed on Fig. 8(b).

4.3. *Stability diagram*

The experimental and numerical results concerning the 3D stability of the cylinder wake are presented for $\alpha = 45°$ (figure 11a) and $\alpha = 60°$ (figure 11b). The same trend is observed for these two angles. At large Froude number, the critical Reynolds number for the mode A tends to 190 as it is the case for a homogeneous fluid. There is a region for moderate stratification ($2 \leqslant F \leqslant 4$), where the mode A is stable and where the mode S is unstable. However, the mode A is always observed at large Reynolds number. This indicates that the mode A is always dominant with respect to the mode S when it is unstable.

For small Froude number ($F \leqslant 1.5$), the critical Reynolds number strongly increases for strong stratification. The von Karman street can be observed without a 3D structure

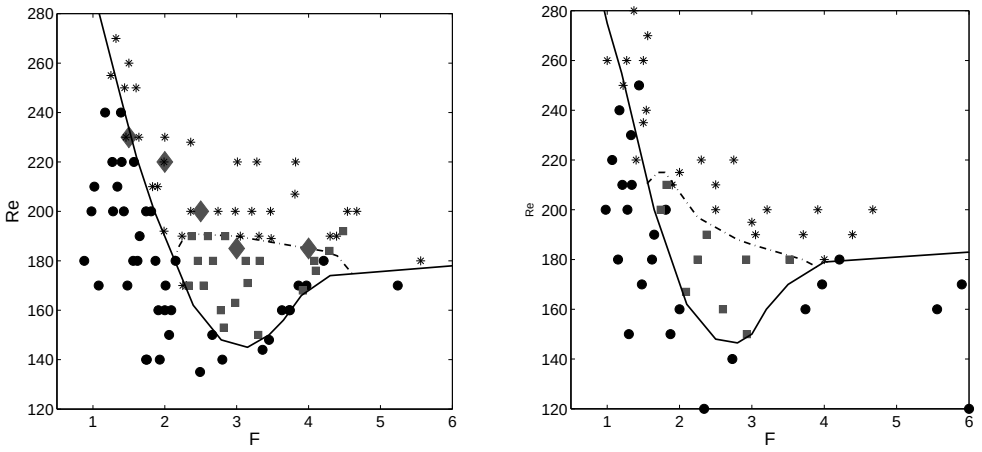

(a) (b)

FIGURE 11. Stability diagrams of a cylinder wake tilted (a) at $\alpha = 45°$ and (b) at $\alpha = 60°$ for different Reynolds and Froude numbers. Black round symbols correspond to stable experiments, stars correspond to the mode A and grey square symbols correspond to the mode S. The transition between a stable and unstable domain is represented by a black line and the mode S / mode A transition is represented by a grey dashed line. The grey diamonds correspond to the critical Reynolds number obtained numerically.

up to Re = 250. It highlights the fact that the wake is strongly stabilized by a strong stratification. However, the small dimensions of the tank used in the experiments do not allow to study very small Froude numbers. Indeed, it would require large cylinder diameters, which would reduce the aspect ratio below 10, leading to strong end effects. It is thus unclear what other instabilities would appear for very small Froude numbers ($F < 0.1$) where a Zig-Zag instability might be observed (Deloncle *et al.* 2011).

The critical Reynolds number has been calculated numerically at $\alpha = 45°$. It seems to be close to the value where the mode A appears in the experiments. This indicates that the mode S hasn't been observed numerically. This is probably due to the weak spatial resolution used when the 3D perturbation is calculated. This introduces a strong numerical diffusion which tends to attenuate the critical layers and thus damp the mode

S. Moreover, these numerical simulations become very noisy when the tilt angle increases. They have not been done for tilt angles larger than 45°.

5. Mode Rayleigh Taylor

In this section, the case of very large tilt angle ($\alpha \in [60°, 85°]$) and large Froude number (i.e weak stratification) is studied.

5.1. *Shadowgraph study*

For nearly horizontal cylinders, a new instability appears at weak stratification. Top shadowgraph views are presented Fig. 12 for a Reynolds number $\mathrm{Re} \simeq 180$ and a Froude number $\mathrm{F} \simeq 8.5$. Under the threshold, straight layers can be seen as in the case of the mode S. Above the threshold these layers are deformed by counter-rotating vortices, creating rolls oriented along the (Ox) axis, similar to the plumes appearing in Rayleigh-Taylor instabilities. This is why this mode has been called mode RT.

This mode is characterized by counter-rotating vortices behind the cylinder as was observed for the mode A. But this new instability presents some differences. First, the tails of the vortices seem to be stretched in the opposite direction (i.e. downstream for this mode and upstream for the mode A). Then, these counter-rotating vortices are very far from the cylinder: they appear about 15 diameters downstream of the cylinder whereas the mode A used to appear 4 diameters downstream. Finally, the dimensionless wavelength $\lambda/D \simeq 3$ is smaller than the wavelength of the mode A ($\lambda/D \simeq 4$), although it is not extremely periodic.

5.2. *Structure of the base flow*

A 2D numerical study has been used to check if the base flow may be unstable with respect to the Rayleigh-Taylor instability. The absolute density of the 2D base flow

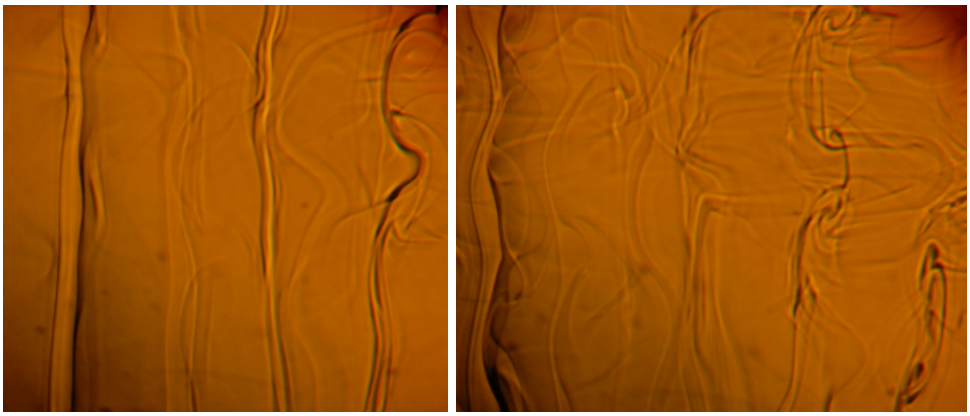

(a) (b)

FIGURE 12. Top shadowgraph visualizations of the wake behind a cylinder tilted at $\alpha = 75^\circ$ with respect to the vertical. The pictures are obtained at Re = 175 and $F = 8.5$. The picture (b) is obtained a time delay $3D/U$ after the picture (a) which is obtained 6 D/U downstream of the cylinder. The cylinder is going to the left. The field of view is approximately 8 by 15 diameters.

$\rho_{\text{abs}} = \rho_{\text{2D}} + \bar{\rho} = \rho_{\text{2D}} + y \sin\alpha$ has been plotted in a nearly vertical plane (see figure 13). In this figure, heavy (resp. light) mushrooms appear, due to the advection of heavy (resp. light) fluid by the von Karman vortices. These structures highlight the fact that heavier fluid can be located above lighter fluid. This overturning of the mean density is unstable with respect to the Rayleigh-Taylor (gravitational) instability. Since these heavy/light mushrooms are invariant along the z direction (see 3D drawing in Fig. 13), they can be subject to an instability with a large axial wavelength. This leads to convective rolls perpendicular to the (Oz) direction, i.e. oriented along the (Ox) axis (see 3D sketch of Fig. 13). This is exactly what has been observed in the shadowgraph visualization of Fig. 12.

The mode RT appears far from the cylinder because it is due to the overturning. Indeed, the density diffuses much slower than the vorticity such that the base flow remains unstable over large downstream distances. By contrast, the mode A is localized very close

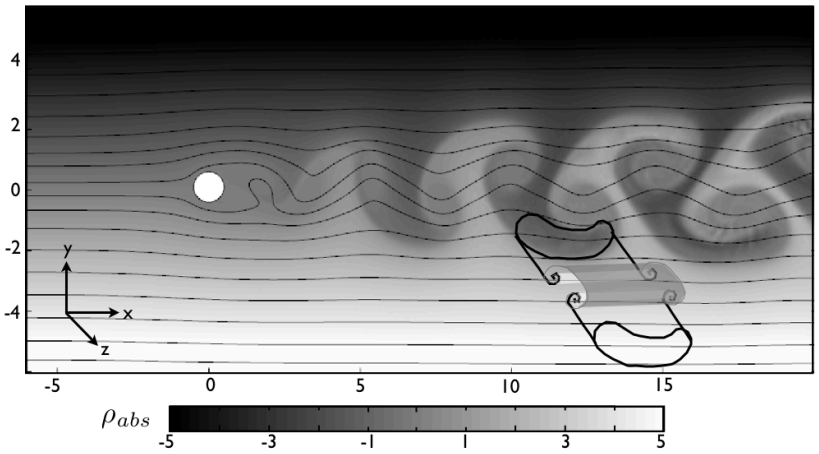

FIGURE 13. Absolute density $\rho_{\text{abs}} = \rho_{\text{2D}} + \bar{\rho}$ of the base flow obtained numerically for a cylinder with a tilt angle $\alpha = 75^\circ$ and for a Re = 170 and F = 8. Solid lines correspond to the streamlines of the 2D flow (u, v) corresponding to a von Karman street. The field of view is 16 by 6 diameters.

to the cylinder because it is driven by the velocity of the vortices which decreases rapidly at these Reynolds numbers.

5.3. *Stability diagram*

The experimental results concerning the 3D stability of the cylinder wake for $\alpha = 75^\circ$ are presented in figure 14. The mode RT appears for very weak stratifications since it has been visualized for Froude numbers as large as 12. The critical Reynolds number is of the order of 180 for moderate Froude numbers ($F \simeq 3$) and decreases down to 150 for large Froude numbers. It thus seems that when the stratification becomes weaker the mode RT becomes more unstable. This is surprising because the mode RT is linked to the density differences of the mushroom structures which should increase with the background density gradient. However, it is possible that at moderate Froude numbers, the background stratification prevents overturning which suppresses the Rayleigh-Taylor instability. This is coherent with the complete suppression of von Karman vortices by the stratification, which occurs for example at $F = 1.7$ for Re = 150 (Meunier 2012).

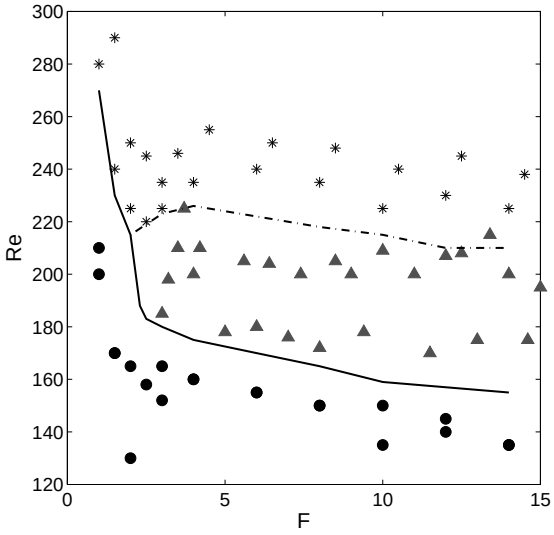

FIGURE 14. Stability diagram for a cylinder wake tilted at $\alpha = 75°$. Black circular symbols (●) correspond to stable experiments, grey triangles (▲) correspond to experiments where the mode RT is observed and stars (∗) correspond to mode A. The stable and unstable domains are separated by a black dashed line and the separation between the mode RT and the mode A is plotted with a dash-dotted line.

At this tilt angle, the mode A can still be visualized but it is not the first unstable 3D mode. It appears for a critical Reynolds number varying from $\mathrm{Re} \simeq 220$ to $\mathrm{Re} \simeq 190$ when the Froude number increases from 2 to 12, which is slightly above the critical Reynolds number of the mode RT. However, the mode A seems to be dominant compared to the mode RT (when it is unstable), probably because the mode A is located very close to the cylinder.

6. Mode L

In this section, the cylinder is still tilted with an angle close to $\alpha = 75°$ but the fluid is now strongly stratified ($0.1 \leqslant \mathrm{F} \leqslant 1$).

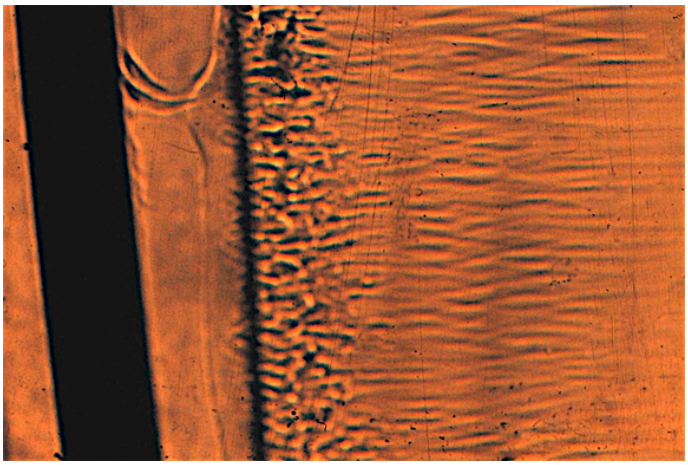

FIGURE 15. Top shadowgraph visualization for Re = 110, $F = 0.55$ and $\alpha = 75^{\circ}$. The cylinder is going to the left of the picture. The field of view is approximately 8 by 15 diameters.

6.1. *Experimental visualizations*

Figure 15 presents the shadowgraph view of the instability appearing for a Reynolds number Re = 110 and a Froude number $F = 0.55$. In this image, a uniform zone is observed just behind the cylinder which extends over 1 diameter. A dark axial line separates this zone from a highly disturbed region, with small-scale structures which give rise further downstream to thin streamwise lines. The wavelength of this instability is dramatically smaller compared to the previous modes since it is of the order of 0.3 diameters (which is 10 times smaller than the wavelength of mode A or mode S). It should be mentioned that the cylinder seems to be tilted in this image, but this is simply due to a deformation by the lens of the shadowgraph.

An important aspect of this unstable mode is that it can appear in the absence of von Karman vortices in the base flow. This is totally different from the three other modes which rely on the presence of von Karman vortices. Indeed, a dye visualization of the 2D base flow has been done at the same parameters where this mode is observed (Re = 110, $F = 0.55$). As can be seen on the side view of figure 16, the 2D base flow does not contain

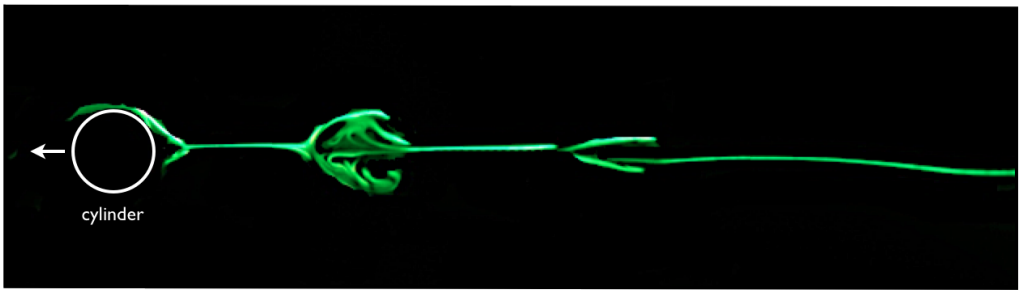

FIGURE 16. Dye visualization from the side of the tank for the same Reynolds number Re = 110 and Froude number F = 0.55 at an angle $\alpha = 75^\circ$ as in figure 15. The cylinder is going to the left of the picture. The field of view is approximately 3 by 15 diameters in the sideview.

a von Karman vortex street. In this image, the recirculation bubble present behind the cylinder is very short. But there is a second recirculation bubble about 1.5 diameter downstream of the cylinder. This in agreement with the visualisations of Boyer *et al.* (1989) who called these bubbles isolated mixed regions. We also observe a small third recirculation bubble further downstream.

Comparing figure 15 and figure 16 indicates that the thick dark axial line of the shadowgraph visualizations is located very close to the upstream end of the second recirculation bubble. It means that the 3D instability is generated near the upstream stagnation point of the recirculation bubble. This is not surprising since the streamwise velocity vanishes at this point, such that any convective instability may become absolutely unstable close to this point.

6.2. *A numerical clue*

In order to understand the origin of this mode, some 2D numerical simulations have been carried out to characterize the base flow. Figure 17 represents the axial velocity w_{2D} obtained numerically for Re = 110, $F = 0.65$ and $\alpha = 75^\circ$, i.e. where the mode L has been visualized. The streamlines undulate downstream of the cylinder because of the lee waves, which propagate at an angle of about 30 degrees with respect to the x

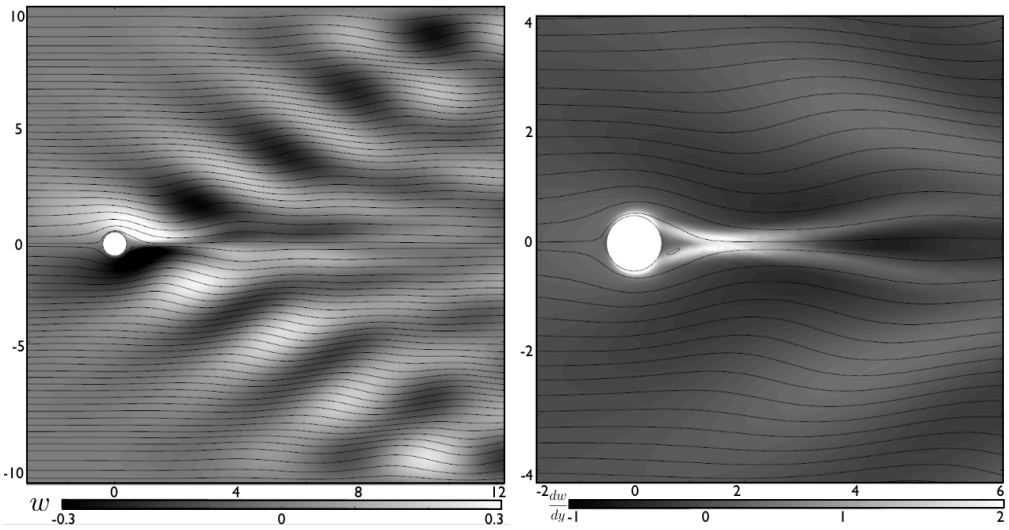

(a) (b)

FIGURE 17. Numerical simulations for a tilt angle $\alpha = 75^\circ$ at Re = 110 and F = 0.65. The greyscales represent in (a) the axial velocity w_{2D} and in (b) the derivative of the axial velocity $\partial w_{2D}/\partial y$. Dark lines correspond to the streamlines.

axis. However, since the cylinder is tilted, these lee waves contain some axial velocity (Meunier 2012b), which is visible as an alternation of white and black lobes along 2 oblique directions.

These axial velocities obviously create a strong shear $\partial w_{2D}/\partial y$ as indicated in figure 17(b). The shear is particularly large on the centerline between the first and second recirculation bubbles, where it is of the order of $2U/D$. This shear may thus be unstable with respect to the Kelvin-Helmholtz instability. This would indeed generate Kelvin-Helmholtz billows oriented along the x axis, which could correspond to the thin streamwise lines visible in Fig. 15. However, estimating the thickness of the shear layer as $\delta \simeq D/2$ allows to deduce an estimate of the wavelength $\lambda \simeq 3D$ corresponding to the most unstable wavelength of the Kelvin-Helmholtz instability. This wavelength is 10 times larger than the wavelength observed in the experiment ($\lambda \simeq 0.3D$). This difference may probably be

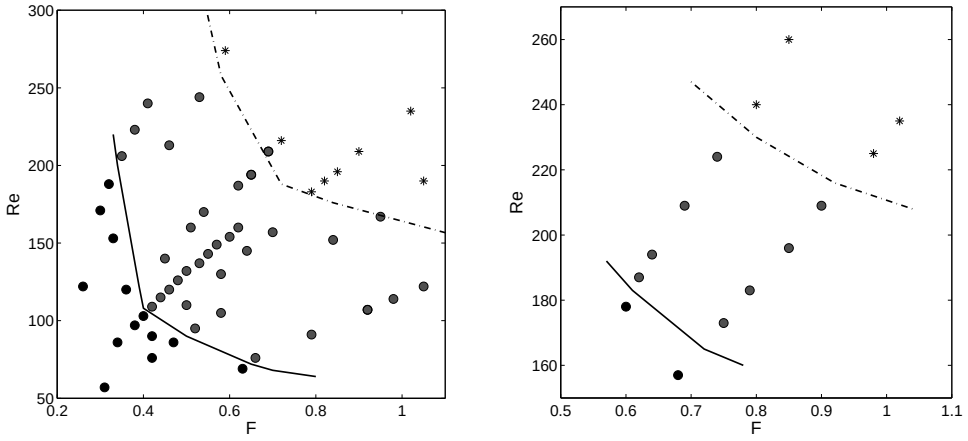

(a) (b)

FIGURE 18. Stability diagrams for strong stratifications and large tilt angles $\alpha = 75°$ (a) and $\alpha = 82.5°$ (b). Dark disks correspond to stable experiments, grey disks correspond to experiment with the mode RT and stars correspond to experiments with the mode A.

due to the hyperbolic point located at the second recirculation bubble which may largely modify the characteristics of the Kelvin-Helmholtz instability.

6.3. *Stability diagram*

The stability diagrams, for $\alpha = 75°$ (figure 18a) and for $\alpha = 82.5°$(figure 17b) have been established at very small Froude numbers ($F \leqslant 1$). The mode L is represented by grey disks. It has been observed for relatively small Reynolds numbers compared to the other unstable modes. Indeed, it can be observed for Reynolds numbers as low as 60 for $\alpha = 75°$.

As for the other modes, the mode A is observed at larger Reynolds numbers (represented as stars on the diagrams). It should be noted that the mode L does not appear for very small Froude numbers ($F < 0.4$ at $\alpha = 75°$). This is surprising because lee waves are expected to be present at very small Froude numbers.

This mode has not been observed for a horizontal cylinder. This is probably due to the

lack of axial velocity in the lee waves at $\alpha = 90°$ (due to the symmetry of the problem). This mode is already more stable at $\alpha = 82.5°$ than at $\alpha = 75°$, as can be inferred by comparing Figs 18(a) and 18(b). This mode is thus limited to nearly horizontal but tilted cylinders ($65° < \alpha < 85°$).

7. Conclusion

In this paper, an experimental study has been delineated of a stratified wake of a circular cylinder in order to describe the effect of the tilt and of the stratification on the 3D instabilities of the wake.

Primarily, it was shown that the classical mode A, well-known in homogeneous cylinder wakes, remains present for weak stratifications (i.e. for large Froude numbers). This mode is made of counter-rotating vortex pairs which appear close to the cylinder. The dimensionless wavelength of this mode is close to 4 as for homogeneous fluids and is independent of the Froude number. Although for weak stratification the critical Reynolds number is close to 190 (as for homogeneous fluids), this mode appears at a smaller Reynolds number for moderate stratifications if the cylinder is nearly vertical. This destabilization seems to be in contradiction with the stabilization of the elliptical instability (which is at the origin of mode A) by the stratification predicted theoretically by Kerswell (2002). However, the mode A is stabilized by a strong stratification. A numerical study has been done, showing a good agreement between the experimental and numerical critical Reynolds numbers.

Figure 19 presents the critical Reynolds number at which the wake becomes three-dimensional for all Froude number F and tilt angle α. The mode A is the first unstable mode for a large range of Froude numbers ($0.1 \leqslant F \leqslant 10$) but only for small tilt angles ($0° \leqslant \alpha \leqslant 60°$).

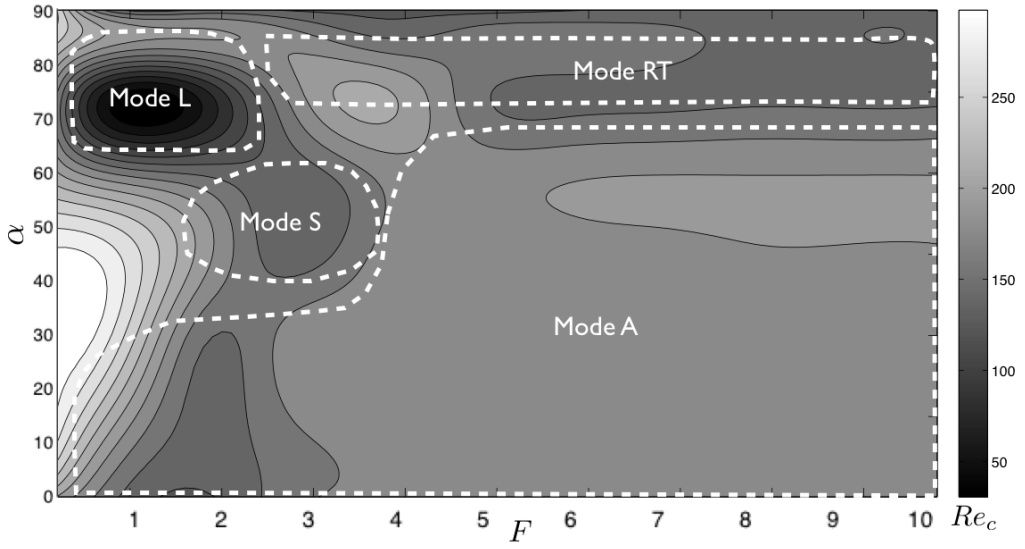

FIGURE 19. Critical Reynolds number Re_c of appearance of a 3D unstable mode as a function of the tilt angle α and the Froude number F. White contours indicate the first unstable mode.

For moderate tilt angles a new unstable mode, called mode S, appears at moderate stratification. This mode, characterized by dark and bright undulated layers, reveals the presence of co-rotating vortices. A 2D numerical study, coupled to the theoretical structure of critical layers inside each von Karman vortex, has shown that these co-rotating vortices are simply Kelvin-Helmholtz billows of the strong shears generated by the axial velocity of the 2D flow. This is similar to the tilt-induced instability of a solitary vortex tilted with respect to the stratification (Boulanger *et al.* 2007). As shown in Fig. 19, the mode S appears in a very narrow region of parameters, i.e. for moderate stratification ($1.5 \leqslant \mathrm{F} \leqslant 3.5$) and moderate tilt angles ($40° \leqslant \alpha \leqslant 70°$).

For large tilt angles ($65° < \alpha < 85°$), two other unstable modes have been discovered (see Fig. 19). For a weak stratification ($3 < F < 10$), shadowgraph visualisations reveal the presence of counter-rotating vortices far from the cylinder. These vortices seem to be convective rolls created by a Rayleigh-Taylor (gravitational) instability. This explanation

is confirmed numerically by the presence of overturning generated by the 2D base flow. This mode has thus been called mode RT.

For large tilt angles and for strong stratifications, the dynamics is strongly modified since three-dimensional instabilities appear even in the absence of von Karman vortices, i.e. for a stationary flow. This mode is due to the presence of lee waves emitted by the cylinder, which contain some axial velocity if the cylinder is tilted. It leads to a strong shear on the centerline downstream of the cylinder which creates streamwise Kelvin-Helmholtz billows. This mode, which has been called mode L (for lee waves mode), is characterized by a very small axial wavelength of the order of 0.3 diameter. This mode is observed for small Froude numbers ($0.4 < F < 2$) and nearly horizontal but tilted cylinders, as shown on Fig. 19.

These results highlight the fact that the stratification strongly modifies the transition from a 2D to a 3D flow in a cylinder wake, with the presence of 3 new unstable modes. The tilt of the cylinder with respect to the vertical plays a major role, such that a study limited to a vertical or a horizontal cylinder misses a lot of the rich dynamics of the tilted wake.

This is particularly interesting for geophysical applications where stratified wakes have been usually restricted to 2D horizontal bluff bodies. For example, in oceans, the wake of a coastal tip may be influenced by the weak inclination of the continental slope such that the wake may become unstable with respect to the mode L instead of being unstable with respect to the mode A as for a horizontal object. The structure of the unstable mode leads to different characteristics (wavelength, orientation of the structures) which may lead to very different mixing and turbulent stresses.

However, because this study is limited to a fundamental bluff body like the cylinder, it is very far from real geophysical applications. It would be interesting to see whether

the rich dynamics described in this paper is still present in the wake of a ridge or a half-cylinder on a tilted plane. The presence of the boundary will modify the structure of the von Karman wake, which may suppress some unstable modes but also create some new unstable modes. Moreover, the presence of the boundary layer on the tilted plane may also modify the whole dynamics of the stratified wake.

In fact, stratified boundary layers over a tilted bottom have received little attention and deserve more work. Candelier *et al.* (2012) have shown theoretically that they are subject to a radiative instability which may be more unstable than the destabilization of the Tolmien-Schlichting waves. Moreover, Passaggia *et al.* (2013) have recently shown numerically that an undulation of the topography generates a critical layer inside the boundary layer, with strong cross-stream flows. It is clear that experiments are needed to confirm and characterize these complex phenomena. To this end, a new tank is being built in our laboratory, which will allow to study the boundary layer of a tilted plane in a background stratification.

Finally, there has been very few numerical studies on the stratified wake of a tilted cylinder. The 2D dynamics has been characterized by Meunier (2012) but the 3D dynamics has never been studied in detail. High level Floquet analysis and Direct Numerical Simulations would probably give more information on the structure and the mechanism of the unstable modes.

Acknowledgements

The authors would like to thank Dr Justin Leontini who helped writing the numerical procedure for the 3D linear stability analysis. This study has been done under the grant ANR 11 BS56 012 01 from the French government.

Appendix A. Calculus of the global growth rate of the elliptic instability for a Gaussian stratified vortex

In this appendix, the details of the calculus evoked in section 3 concerning the mode A are developed. This calculus has the purpose of verifying the local theory given by Kerswell (2002) for the growth rate of the elliptic instability in a stratified fluid. An inviscid study is done here using a global approach analyzing the coupling of Kelvin modes via the ellipticity.

A.1. *Definition of the velocity and calculus of the elliptical base flow*

The question is to know if a 2D stratified and vertical vortex with elliptic streamlines can be unstable with respect to a 3D perturbation $\mathbf{u}'$ which grows in time with a growth rate σ. The total velocity is thus decomposed into 3 terms

$$\mathbf{u}_{\text{tot}} = \mathbf{u} + \epsilon \mathbf{u}_{\text{ell}} + \mathbf{u}' \tag{A 1}$$

where the 2D base flow is the sum of an axisymmetric vortex $\mathbf{u}$ and a small ellipticity $\epsilon \mathbf{u}_{\text{ell}}$. The axisymmetric vortex is characterized by its angular velocity $\Omega(r)$ such that the velocity is written in cylindrical coordinates

$$\mathbf{u} = (u, v, w) = (0, r\Omega(r), 0).$$

The theory is developed for any angular velocity profile. But in the numerical treatment, the vortex is supposed to have a Gaussian vorticity profile, characterized by an angular velocity equal to $\Omega(r) = (1 - e^{-r^2})/r^2$. This supposes that the equations are dimensionalized using the core size and the inverse of the angular velocity at the center $\Omega(0)^{-1}$ for lengths and times. This defines the Froude number of the vortex as

$$F_V = \Omega(r = 0)/N,$$

N being the Brunt-Väisälä frequency.

The elliptical deformation $\epsilon \mathbf{u}_{\rm ell}$ of the vortex is characterized by an azimuthal wavenumber equal to 2. The incompressibility condition imposes that it is of the form

$$\mathbf{u_{ell}} = [rf(r)\cos(2\theta), -(rf(r) + r^2 f'(r)/2)\sin(2\theta), 0]. \quad \text{(A 2)}$$

The strain $f(r)$ must satisfy a differential equation in order for the base flow to be a solution of the Euler equations. This equation is rather found by introducing the decomposition $\zeta_{\rm tot} = \zeta + \epsilon\zeta_{\rm ell}$ of the axial component of the vorticity into the vorticity equation:

$$\frac{\partial \zeta_{\rm tot}}{\partial t} + (\mathbf{u}_{\rm tot} \cdot \nabla)\zeta_{\rm tot} = \mathbf{0}$$

The definition of the axial vorticity $\zeta_{\rm ell} = \partial(rv_{\rm ell})/r\partial r - \partial u_{\rm ell}/r\partial\theta$ leads, at first order in ϵ and for $u' = 0$ to

$$f''(r) + \frac{5f'(r)}{r} - \frac{\zeta(r)}{r\Omega(r)}f(r) = 0$$

where $\zeta(r) = 2\Omega + rd\Omega/dr$ is the vorticity of the base flow. This equation is numerically solved using Matlab with $f(0) = 1$, $f'(0) = 0$. This means that ϵ corresponds to the strain at the center of the vortex. The strain is plotted in Fig. 20 and exactly corresponds to the plot given by Eloy & Le Dizès (1999) in their figure 1. It shows that the strain at infinity is smaller by a factor 2.52 compared to the strain at the center of the vortex.

A.2. *ϵ= 0: Stratified Kelvin modes*

In the absence of ellipticity ($\epsilon = 0$), the 3D perturbations satisfying the Euler equations are the Kelvin modes. Their structure is well-known for a homogeneous fluid. We derive here the calculation with a linear stratification so as to do the numerical resolution for the growth rate in the next section. The perturbation $\mathbf{u}'$ is searched as a Kelvin mode characterized by an axial wavenumber k, an azimuthal wavenumber m and a frequency ω:

$$\mathbf{u}' = \mathbf{u_k}(r)e^{ikz+im\theta-i\omega t} + c.c$$

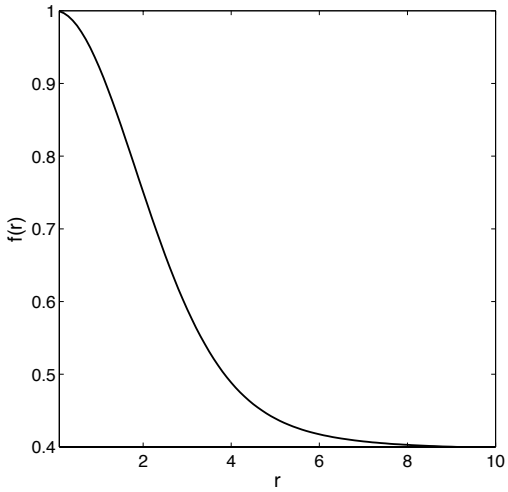

FIGURE 20. Radial profile of the strain $f(r)$ in a vortex with a Gaussian vorticity deformed elliptically by the flow (A 2).

where c.c. is the complex conjugate.

Introducing this form in the Navier-Stokes and density equations (2.1) and linearizing around the base flow leads for $\epsilon = 0$ to

$$-i(\omega - m\Omega)u_k - 2\Omega v_k = -p_k' \tag{A 3a}$$

$$-i(\omega - m\Omega)v_k + \zeta u_k = \frac{-imp_k}{r} \tag{A 3b}$$

$$-i(\omega - m\Omega)w_k = -ikp_k - \rho_k \tag{A 3c}$$

$$\frac{1}{r}\partial(ru_k)\partial r + \frac{im}{r}v_k + ikw_k = 0 \tag{A 3d}$$

$$-i(\omega - m\Omega)\rho_k = \frac{w_k}{F_V^2}. \tag{A 3e}$$

It is recalled that $\zeta = 2\Omega + r\Omega'$ is the vorticity of the axisymmetric vortex. As previously, the equations have been dimensionalized by the core size and the inverse of the angular velocity at the center. Moreover, the density has been dimensionalized by ρ_0. The calculus is made in the inviscid case, with $\mathrm{Re} = \infty$. After some algebra, the velocity and the density can be written as a function of p_k:

$$u_k = \frac{2im\Omega p_k/r - i\omega p_k'}{\omega^2 - 2\Omega\zeta}$$
$$v_k = \frac{m\omega p_k/r - \zeta p_k'}{\omega^2 - 2\Omega\zeta}$$
$$w_k = \frac{k\omega p_k}{\omega^2 - F_V^{-2}}$$
$$\rho_k = \frac{ikp_k}{\omega^2 F_V^2 - 1}.$$

Reintroducing these expressions into (A 3d) leads to a differential equation for the pressure p_k

$$p_k'' + \left(\frac{1}{r} - \Delta\Delta'\right) p_k' + \left[\frac{2m}{r\varpi}(\Omega' - \frac{\Omega\Delta'}{\Delta}) - \frac{k^2\Delta}{F_V^{-2} - \varpi^2} - \frac{m^2}{r^2}\right] p_k = 0$$

where $\Delta(r) = \phi - \varpi^2$ with $\varpi = -\omega + m\Omega(r)$ the Doppler shifted frequency and $\phi = (1/r^3)\partial(r^4\Omega^2)/\partial r$ the Rayleigh discriminant. In the numerics, the Rayleigh discriminant is equal to $\phi = 4e^{-r^2}(1 - e^{-r^2})/r^2$. This differential equation can be derived from the differential equation (6) of Billant & Le Dizès (2009) for $\Psi = p_k/\varpi$.

This differential equation is solved numerically by Matlab, using the boundary conditions $p_k(0) = 0$, $p_k'(0) = 1$. For each frequency ω, there is a discrete number set of wavenumbers k for which the pressure vanishes at infinity. These solutions correspond to the Kelvin modes for this stratified Gaussian vortex. The wavenumbers are found numerically by minimizing the value of the pressure at $r = 5$. For $\omega = 0$ and $m = 1$, the first wavenumber k is equal to 2.326 for $F_V = 11.1$. The solution for the velocity and the pressure are plotted in Fig. 21 for this Froude number. They are similar to the functions plotted in Eloy & Le Dizès (1999) for $F_V = +\infty$.

In the following, two Kelvin modes will be coupled by the ellipticity. As will be shown in the next section, this is possible for $m = \pm 1$ and $\omega = 0$. For each Froude number, the wavenumber k is thus searched numerically and the velocity and density of the Kelvin

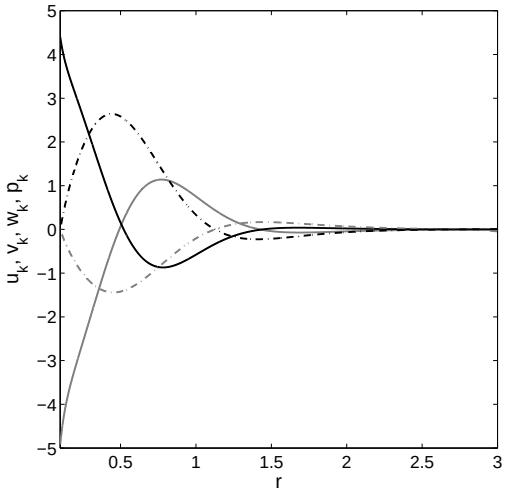

FIGURE 21. Radial profile of the three velocity components (u_k, v_k, w_k) and of the pressure term p_k obtained for a Kelvin mode characterized by $m = 1$, $k = 2.326$, $\omega = 0$ and for a Froude number $F_V = 11.1$.

modes are then computed numerically. However, it should be mentioned that the Kelvin modes can only be calculated for small stratifications (large Froude numbers) since the critical points (where $F_V^{-2} - \varpi^2$ vanishes) get closer to the center of the vortex at moderate Froude numbers and prevent the numerical integration of the differential equation.

A.3. *Triadic resonance of 2 Kelvin modes* ($\epsilon \neq 0$)

The elliptic instability can be seen as a triadic resonance between two Kelvin modes and the ellipticity. Indeed, the ellipticity contains a Fourier component of axial wavenumber $k = 0$, azimuthal wavenumber $m = 2$ and a frequency $\omega = 0$ which can couple different Kelvin modes via the nonlinear term of the Navier-Stokes equations. The two Kelvin modes are characterized by their axial wavenumbers k_1 and k_2, azimuthal wavenumber m_1 and m_2 and frequencies ω_1 and ω_2. The perturbation is searched as a sum of two

Kelvin modes of amplitude A_1 and A_2 which grow slowly in time with a growth rate $\epsilon\sigma$:

$$\mathbf{U}' = A_1\mathbf{V}_{k1} + A_2\mathbf{V}_{k2} = [A_1\mathbf{U}_{k1}(r)e^{ik_1z+im_1\theta-i\omega_1t} + A_2\mathbf{U}_{k2}(r)e^{ik_2z+im_2\theta-i\omega_2t}]e^{\epsilon\sigma t} + c.c \tag{A 4}$$

In this section, upper case bold letters $\mathbf{U}$ correspond to the penta-vector (u, v, w, ρ, p). Moreover, $\mathbf{U}_{k1}$ and $\mathbf{U}_{k2}$ are penta-vectors depending only on r, whereas $\mathbf{V}_{k1}$ and $\mathbf{V}_{k2}$ also contain the axial, azimuthal and temporal dependence. The problem is to determine the growth rate σ of the perturbation in the presence of a small elliptic flow $\epsilon \neq 0$.

Introducing the perturbation (A 4) into the Navier-Stokes equations (2.1) and neglecting the viscous terms and the non linear terms A_1^2, A_2^2 and A_1A_2 leads at first order in ϵ to:

$$\epsilon\sigma(A_1\mathbf{V}_{\mathbf{k_1}}+A_2\mathbf{V}_{\mathbf{k_2}}) = -(\mathbf{V}_{\rm ell}.\nabla)A_2\mathbf{V}_{k_2}-A_2(\mathbf{V}_{k_2}.\nabla)\mathbf{V}_{\rm ell}-(\mathbf{V}_{\rm ell}.\nabla)A_1\mathbf{V}_{k_1}-A_1(\mathbf{V}_{k_1}.\nabla)\mathbf{V}_{\rm ell} \tag{A 5}$$

where $\mathbf{V}_{\rm ell} = \epsilon(u_{\rm ell}, v_{\rm ell}, 0, 0, 0)$ is the penta-vector of the elliptic flow.

This linear equation for $\mathbf{V}_{k1}$, $\mathbf{V}_{k2}$ can be written in terms of a matrix $\mathbb{N}$ by making $\mathbf{V}_{\rm ell}$ explicit. It leads to:

$$\epsilon\sigma(A_1\mathbf{V}_{k1} + A_2\mathbf{V}_{k2}) = \epsilon(e^{2i\theta}\mathbb{N}_{m_1} + e^{-2i\theta}\bar{\mathbb{N}}_{m_1})\mathbf{V}_{k1} + \epsilon(e^{2i\theta}\mathbb{N}_{m_2} + e^{-2i\theta}\bar{\mathbb{N}}_{m_2})\mathbf{V}_{k2} \tag{A 6}$$

where $\mathbb{N}_m$ is the following matrix:

$$\mathbb{N}_m = \begin{pmatrix} \alpha & \beta & 0 & 0 & 0 \\ \gamma & \delta & 0 & 0 & 0 \\ 0 & 0 & \chi & 0 & 0 \\ 0 & 0 & 0 & \chi & 0 \\ 0 & 0 & 0 & 0 & 0 \end{pmatrix}$$

with

$$\begin{cases} \alpha = rf(r)\partial_r/2 - (rf'(r)/2 + f(r))m/2 + (rf'(r) + f(r))/2 \\ \beta = rf(r)/2i \\ \gamma = -[(5r/2 - \alpha r^2/2)f'(r) + (2 - \beta r^2/2)f(r)]/2i \\ \delta = -(rf'(r) - f(r))/2 + rf(r)\partial_r/2 - (rf'(r)/2 + f(r))m/2 \\ \chi = rf(r)\partial_r/2 - (rf'(r)/2 + f(r))m/2 \end{cases}$$

There can be a triadic resonance if the term $e^{2i\theta}\mathbb{N}_{m_1}\mathbf{V}_{k1}$ has the same Fourier component as the second Kelvin mode. In this case, the term $e^{-2i\theta}\bar{\mathbb{N}}_{m_2}\mathbf{V}_{k2}$ has the same Fourier component as the first Kelvin mode. There is thus a mutual growth of the two Kelvin modes due to the non-linear coupling with the ellipticity. The resonance conditions are simply:

$$(k_2 = k_1, m_2 = m_1 + 2, \omega_2 = \omega_1).$$

As previously mentioned, this is obtained for $m_1 = -1$ and $m_2 = 1$ with $\omega = 0$ due to the symmetry of the dispersion relation of the Kelvin modes. This defines the wavenumber for each Froude number, which is used to compute numerically the profiles of the Kelvin modes.

If the resonance conditions are satisfied, the Fourier component $e^{ik_1z+im_1\theta-i\omega_1t}$ of equation (A 6) is simply written:

$$\epsilon\sigma A_1\mathbf{U}_{k1} = \mathbb{N}_{-1}A_2\mathbf{U}_{k2} \tag{A 7}$$

where $\mathbf{U}_{k1}$ and $\mathbf{U}_{k2}$ are penta-vectors depending only on r. Instead of solving this

matrix equation, we define a scalar product:

$$\langle \mathbf{U}_i | \mathbf{U}_j \rangle = \int_{r=0}^{+\infty} (\bar{u}_i u_j + \bar{v}_i v_j + \bar{w}_i w_j + F_v^2 \bar{\rho}_i \rho_j) r dr$$

for which the linear operator of the Kelvin modes is self-adjoint. Multiplying equation (A 7) by $\langle \mathbf{U}_{\mathbf{k_1}} |$ leads to

$$\sigma A_1 = N_{12} A_2 \qquad \text{with} \qquad N_{12} = \frac{\langle \mathbf{U}_{k1} | \mathbb{N} \mathbf{U}_{k2} \rangle}{\langle \mathbf{U}_{k1} | \mathbf{U}_{k1} \rangle}$$

Here N_{12} is a simple integral over r and can be calculated numerically since the components of the Kelvin modes are known numerically. Doing the same reasoning for the Fourier component of the second Kelvin mode leads to

$$\sigma A_2 = \bar{N}_{21} A_1 \qquad \text{with} \qquad \bar{N}_{21} = \frac{\langle \mathbf{U}_{k2} | \bar{\mathbb{N}} \mathbf{U}_{k1} \rangle}{\langle \mathbf{U}_{k2} | \mathbf{U}_{k2} \rangle}$$

Multiplying these two equations leads to the value of the growth rate:

$$\sigma = \sqrt{N_{12} \bar{N}_{21}} \tag{A 8}$$

It can be calculated numerically for each Froude number by computing N_{12} and $\bar{N}_{21}$. This result using the global approach has been plotted in Fig. 22 as grey disks for the first wavenumber and as black disks for the second wavenumber. The prediction is very close to the result found by Kerswell (2002) using a local approach

$$\sigma_{\text{local}} = \frac{9(1 - F_V^{-2})}{16(4 - F_V^{-2})} \epsilon, \tag{A 9}$$

which is plotted as a dash-dotted line. This result tends to $9\epsilon/16$ at large Froude numbers.

The result obtained by Guimbard *et al.* (2010) using a global approach for the flow inside an elliptic cylinder has also been plotted as stars. The growth rate has an analytic expression given by

$$\sigma_{\text{cylinder}} = \frac{9(1 - F_v^{-2})(\varphi^2 + 1)}{12(2 + F_v^{-2}) + 4\varphi^2(4 - F_v^{-2})} \tag{A 10}$$

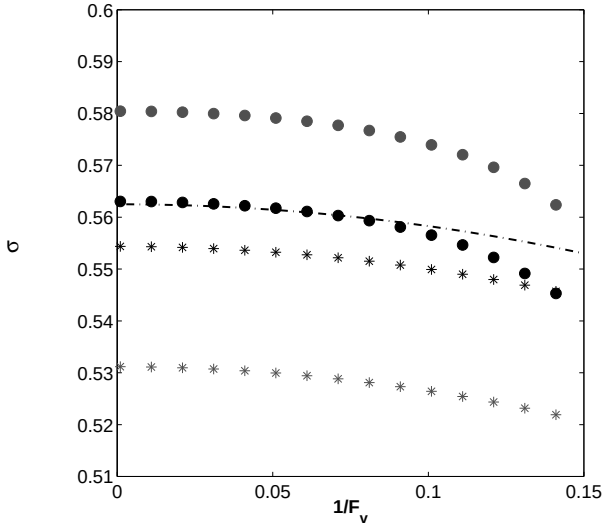

FIGURE 22. Growth rate σ of the elliptic instability for a stratified vortex as a function of the Froude number. Round symbols correspond to the prediction developed in this appendix using the global approach for a Gaussian vortex, with the first (grey symbols) and second (black symbols) Kelvin mode. The black dash-dotted line corresponds to the prediction done by Kerswell (2002) using a local approach (A 9). Stars correspond to the growth rate (A 10) predicted by Guimbard *et al.* (2010) using a global approach for the flow inside a cylinder for the first Kelvin mode (grey symbols) and the second Kelvin mode (black symbols).

where φ is the first (resp. second) root of $J_0(\varphi) + 3J_2(\varphi) = 0$ for the first (resp. second) Kelvin mode plotted as a grey (resp. black) star. J is the bessel function.

All the results are very close (within 6%). Moreover, all the values of the growth rate decrease with the inverse of the Froude number. This indicates that the stratification tends to stabilize the elliptic instability. However, this result is limited to large Froude numbers due to the presence of critical points in the equation of the Kelvin modes. More work would be needed to compute the growth rate at moderate Froude numbers.

REFERENCES

Albarede, P. & Provansal, M. 1995 Quasi-periodic cylinder wakes and the Ginzburg-Landau model. *J. Fluid Mech.* **291** (191-222).

Baines, P. 1987 Upstream blocking and air-flow over mountains. *Annu. Rev. Fluid Mech* **19** (75-97).

Barkley, D. 1996 Three-dimensional Floquet stability analysis of the wake of a circular cylinder. *J. Fluid Mech.* **322** (215-241).

Barkley, D., Tuckerman, L. S. & Golubitski, M. 2000 Bifurcation theory for three-dimensional flow in the wake of a circular cylinder. *Phys. Rev. E* **61**, 5247.

Behara, S. & Mittal, S. 2010 Wake transition in flow past a circular cylinder. *Phys. Fluids* **22**, 114104.

Billant, P. & Le Dizès, S. 2009 Waves on a columnar vortex in a strongly stratified fluid. *Phys. Fluids* **21** (106602).

Bloor, M. S. 1964 The transition to turbulence in the wake of a circular cylinder. *J. Fluid Mech.* **19**, 290.

Boulanger, N., Meunier, P. & Le Dizès, S. 2006 Structure of a stratified tilted vortex. *J. Fluid Mech.* **583** (443-458).

Boulanger, N., Meunier, P. & Le Dizès, S. 2007 Tilt-induced instability of a stratified vortex. *J. Fluid Mech.* **596** (1-20).

Boyer, D. L., Davies, P. A., Fernando, H. & Zhang, X. 1989 Linearly stratified flow past a horizontal circular cylinder. *Philos. Trans. R. Soc. London Ser.* **328** (501).

Browand, F. & Winant, C. 1972 Blocking ahead of a cylinder moving in a stratified fluid: an experiment. *Geophys. Fluid Dyn.* **4** (29-53).

Brucker, K. & Sarkar, S. 2010 A comparative study of self-propelled and towed wakes in a stratified fluid. *J. Fluid Mech.* **652** (373-404).

Canals, M., Pawlak, G. & MacCready, P. 2009 Tilted baroclinic tidal vortices. *J. Phys. Oceanography* **39**, 333–350.

Candelier, J., Le Dizès, S. & Millet, C. 2011 Three-dimensional instability of an inclined stratified plane jet. *J. Fluid Mech.* **685**, 191–201.

Candelier, J., Le Dizès, S. & Millet, C. 2012 Inviscid instability of a stably stratified compressible boundary layer on an inclined surface. *J. Fluid Mech.* **694**, 524–539.

Deloncle, A., Billant, P. & Chomaz, J.-M. 2011 Three-dimensional stability of vortex arrays in a stratified and rotating fluid. *J. Fluid Mech.* **678**, 482–510.

Diamessis, P. J., Spedding, G. R. & Domaradzki, J. A. 2011 Similarity scaling and vorticity structure in high-Reynolds-number stably stratified turbulent wakes. *J. Fluid Mech.* **671**, 52–95.

Dusek, J., Le Gal, P. & Fraunié, P. 1994 A numerical and theoretical study of the first Hopf bifurcation in a cylinder wake. *J. Fluid Mech.* **264** (59-80).

Eloy, C. & Le Dizès, S. 1999 Three dimensional instability of Burgers and Lamb-Oseen vortices in a strain field. *J. Fluid Mech.* **378** (145-166).

Guimbard, D., Le Dizès, S., Le Bars, M., Le Gal, P. & Leblanc, S. 2010 Elliptic instability of a stratified fluid in a rotating cylinder. *J. Fluid Mech.* **660**, 240–257.

Hama, F. R. 1957 Three-dimensional vortex pattern behind a circular cylinder. *J. Aero. Sci.* **24** (156).

Henderson, D. 1997 Nonlinear dynamics and pattern formation in turbulent wake transition. *J. Fluid Mech.* **352**, 65.

Jackson, C. P. 1987 A finite-element study of the onset of vortex shedding in flow past variously shaped bodies. *J. Fluid Mech.* **182** (23-45).

von Karman, T. 1912 Uber den mechanismus den widerstands, den ein bewegter korper in einer flussigkeit erfarht. göttingen nachr. *Math. Phys.* **12** (509).

Karniadakis, G. E. & Triantafyllou, G. S. 1992 Three-dimensional dynamics and transition to turbulence in the wake of bluff objects. *J. Fluid Mech.* **238**, 1.

Kerswell, R. 2002 Elliptical instability. *Annu. Rev. Fluid Mech* **34** (83-113).

Landau, L. & Lifchitz, E. 1971 *Physique théorique: Mécanique*. Editions MIR.

Le Dizès, S. 2008 Inviscid waves on a lamb-oseen vortex in a rotating stratified fluid: consequences on the elliptic instability. *J. Fluid Mech.* **597**, 283–303.

Leweke, T. & Williamson, C. 1998 Three-dimensional instabilities in wake transition. *European Journal of Mech.* **17** (571-586).

Lin, J. T. & Pao, Y. H. 1979 Wakes in stratified fluids: a review. *Annu. Rev. Fluid Mech* **11** (317-338).

Mathis, C., Provansal, M. & Boyer, L. 1984 The Bénard-von Karman instability: an experimental study near the threshold. *J. Phys. Lett.* **45**, 483–491.

Meiburg, E. & Lasheras, J. C. 1988 Experimental and numerical investigation of the three-dimensional transitions in plane wakes. *J. Fluid Mech.* **190** (1-37).

Meunier, P. 2012 Stratified wake of a tilted cylinder. Part 1: Suppression of a von Karman vortex street. *J. Fluid Mech.* .

Meunier, P. 2012b Stratified wake of a tilted cylinder. Part 2: lee internal waves. *J. Fluid Mech.* .

Meunier, P. & Spedding, G. 2004 A loss of memory in stratified momentum wakes. *Phys. Fluids* **16** (298-305).

Meunier, P. & Spedding, G. 2006 Stratified propelled wakes. *J. Fluid Mech.* **552** (229-256).

Noack, B. & Eckelmann, H. 1994 A global stability analysis of the steady and periodic cylinder wake. *J. Fluid Mech.* **270** (297-330).

Norberg, C. 1994 An experimental investigation of the flow around a circular cylinder: influence of aspect ratio. *J. Fluid Mech.* **258**, 287.

Passaggia, P.-Y., Meunier, P. & Le Dizès, S. 2013 Critical layers in the lee waves of a tilted stratified boundary layer. *submitted to J. Fluid Mech.* .

Provansal, M., Mathis, C. & Boyer, L. 1987 Bénard von-Karman instability: transient and forced regimes. *J. Fluid Mech.* **182** (1-22).

Schumm, M., Berger, E. & Monkewitz, P. 1994 Self-excited oscillations in the wake of two-dimensional bluff bodies and their control. *J. Fluid Mech.* **271** (17-53).

Sheard, G., Thompson, M. C. & Hourigan, K. 2003 A coupled Landau model describing the Strouhal Reynolds number profile of a three-dimensional circular cylinder wake. *Phys. Fluids* **15**, L68.

Spedding, G. R. 1997 The evolution of initially turbulent bluff-body wakes at high internal Froude number. *J. Fluid Mech.* **337** (283-301).

Thompson, M., Hourigan, K. & Sheridan, J. 1994 Three-dimensional instabilities in the cylinder wake. *In Intl Colloq. Jets, Wakes, and Shear layers* .

Thompson, M., Hourigan, K. & Sheridan, J. 1996 Three-dimensional instabilities in the wake of a circular cylinder. *Exp. Therm. and Fluid Science* **12** (190-196).

Thompson, M. C., Leweke, T. & Williamson, C. H. K. 2001 The physical mechanism of transition in bluff body wakes. *J. Fluids Struct.* **15**, 607–616.

Williamson, C. 1988 The existence of two stages in the transition to three-dimensionality of a circular cylinder wake. *Phys. Fluids* **31** (3165-3168).

Williamson, C. 1996a Vortex dynamics in the cylinder wake. *Annu. Rev. Fluid Mech* **28** (477-539).

Williamson, C. . H. K. 1996b Three-dimensional wake transition. *J. Fluid Mech.* **328**, 345–407.

Winters, K. B. & Armi, L. 2012 Hydraulic control of continuously stratified flow over an obstacle. *J. Fluid Mech.* **700**, 502–513.

Wu, J., Sheridan, J., Welsh, M. & Hourigan, K. 1996 Three-dimensional vortex structures in a cylinder wake. *J. Fluid Mech.* **312** (201-222).

Xu, Y., Fernando, H. & Boyer, D. 1995 Turbulent wakes of stratified flow past a cylinder. *Phys. Fluids* **7** (2243-2255).

Zhang, H., Fey, U., Noack, B. R., Konig, M. & Eckelmann, H. 1995 On the transition of the cylinder wake. *Phys. Fluids* **7**, 1.